FAULTS AND DISCONTINUITIES ANALYSIS:

APPLICATION TO BARNETT SHALE DATA

A Thesis Presented to

the Faculty of the Department of Earth and Atmospheric Sciences

University of Houston

In Partial Fulfillment

of the Requirements for the Degree

Master of Science

By

Jie Qi

May, 2013

FAULTS AND DISCONTINUITIES ANALYSIS:

APPLICATION TO BARNETT SHALE DATA

_____

Jie Qi

APPROVED:

_____

Dr. John Castagna, Chairman

_____

Dr. Evgeny Chesnokov

_____

Dr. Donald Kouri

_____

Dean, College of Natural Sciences and Mathematics

ACKNOWLEDGEMENTS

My sincerest thanks go to my advisor Dr. John Castagna for sharing his expertise in spectral analysis and fault detection theory and for encouraging my master's work. I would like to thank Dr. Evgeny Chesnokov for teaching me elastic theory and seismic wave theory. I would also like to thank Dr. Donald Kouri for his very helpful suggestions in spectral analysis and for further refining this manuscript. Thanks also to Marathon Oil for the use of their 3D Barnett Shale seismic data donated to the University of Houston and to Allied Geophysical Lab for allowing and encouraging me to use this data for this project. Last, but not least, thanks to my family, especially my fiancée Qinglu Cheng, for their support in achieving this milestone.

FAULTS AND DISCONTINUITIES ANALYSIS:

APPLICATION TO BARNETT SHALE DATA

An Abstract of Thesis

Presented to

the Faculty of the Department of Earth and Atmospheric Sciences

University of Houston

In Partial Fulfillment

of the Requirements for the Degree

Master of Science

By

Jie Qi

May, 2013

ABSTRACT:

Based on the Barnes method of discontinuity filters, I created a new fault-detection attribute and compared it with the constrained least squares spectral analysis (CLSSA) method in Barnett Shale fault detection. The fault-detection attribute is calculated using the Principal Component Analysis (PCA) of different seismic attributes such as coherency, most positive curvature, variance, smoothed seismic data, and also isofrequency phase discontinuities volume. The most positive curvature has better resolution compared with other curvature attributes, while coherency attribute is a very good way to map karst-related structures. Phase spectrum is a good way to detect lateral acoustic discontinuities, while some small discontinuities can be detected very well in the specific frequency phase map. The fault-detection attribute can thus reinforce the similar information of these attributes and reduce the dissimilar information as noise. CLSSA is a better spectral method than the short-time Fourier transform method because it reduces classical spectral smoothing. Spectral analysis can also highlight stratigraphic characterization. Based on these features, the application of fault-detection attribute and CLSSA show better resolution in Barnett Shale fault detection. As compared to coherence and curvature, the resulting PCA fault-attribute better resolves minor tectonic and karst-related fractures.

Table of Contents

1. INTRODUCTION

1.1 Motivation

Faults play an important role in gas and oil exploration and production. They can assist in the formation of hydrocarbon reservoirs, but they can also destroy reservoirs and leak oil and gas. Accurately estimating fault trends could help researchers better understand and interpret underground characteristics in the Barnett Shale area in northeast Texas. Understanding an underground fault system permits better reservoir prediction and estimation.

Barnett Shale hydrocarbon production is very much affected by faults, karst, and fractures because escaping water from the underlying Ellenburger Group could force the release of Barnett Shale gas. Consequently, it is normally necessary to find a Viola-Simpson limestone layer between Barnett and Ellenburger formations because this layer act as a buffer from leakage due to fractures, faults, and Karst.

Fault interpretation is a time-consuming task that requires large amounts of human effect before a consistent earth-model is created; it is also affected by an interpreter's subjective factors. Examination of individual seismic attributes cannot provide enough useful and detailed information. Comparison of many seismic attributes to find differences is inefficient. In addition, traditional seismic attribute methods have

limited application in detecting small faults. We propose two unconventional methods to detect faults using seismic data sets.

1.2 Background

In geology, a fault is a planar fracture or discontinuity in a volume of rock, across which there has been significant displacement along the fractures as a result of earth movement. Large faults within the earth's crust result from the action of plate tectonic forces, such as subduction zones. In geotechnical engineering terms, a fault often forms a discontinuity that may have a large influence on the mechanical behavior (strength, deformation, etc.) of soil and rock masses in, for example, tunnel, foundation, or slope construction. In oil and gas exploration, faults are important structures for reservoir development. The conventional way to pick big faults depends on interpreters' hands-on time. This method is time consuming on reservoir interpretation.

One such reservoir is located within the Barnett Shale formation, located near Fort Worth, Texas (Figure 1, Figure 2). The Barnett Shale (Mississippian age) is the primary source rock for oil and gas that is produced from numerous conventional clastic and carbonate rock petroleum reservoirs of Paleozoic age in the Bend Arch-Fort Worth Basin. It is also the source and reservoir for the tight, siliceous shale gas accumulations. Based on this information, a Barnett-Paleozoic total petroleum system was identified that includes mature Barnett Shale source rock, all known oil and gas accumulation, and an area hypothesized to contain undiscovered oil and gas accumulation (Pollastro *et al.*, 2003). In the Bend Arch-Fort Worth Basin area, the northern, eastern, and southeastern

extent of the Barnett is controlled by structural fronts of the Red River Arch, Muenster Arch, and Ouachita Thrust Front, respectively. The western margin is an erosional limit of facies change along the eastern shelf and Concho Platform. Adjacent to the Muenster Arch, the Barnett Shale is more than 305 meter thick and interbedded with thick limestone. Westward, the Barnett thins rapidly over the Mississippian-age chapel limestone shelf to only a few tens of feet.

Oil and gas are produced from carbonate and clastic rock reservoirs ranging in age from Ordovician to Permian. The Barnett Shale reservoir is made up of dense organic-rich shale, in some areas divided into upper and lower members by the Forestburg Limestone. The overlying Marble Falls Formation is mainly made up of limestone, whereas the underlying Ellenburger Group is comprised of porous dolomite and limestone.

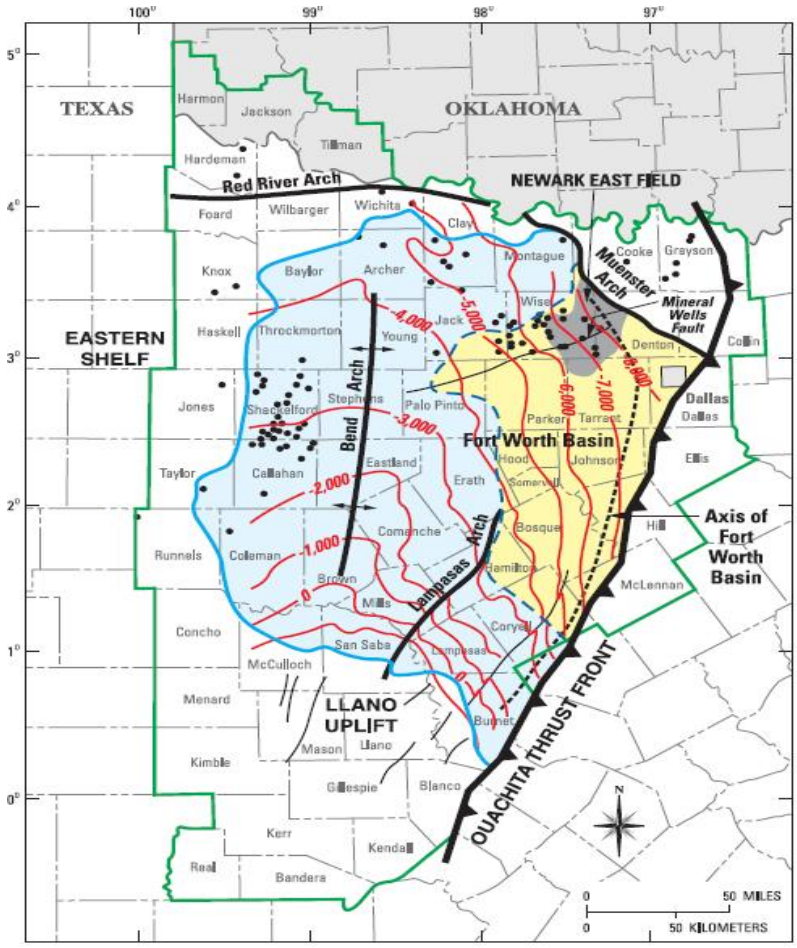

Figure 1. Major structures in the Fort Worth Basin: Muenster Arch, Red River Arch to the north, and Ouachita Thrust Fronts. The western margin is an erosional limit of facies change along the eastern shelf (Modified after Montgomery *et al*. 2005).

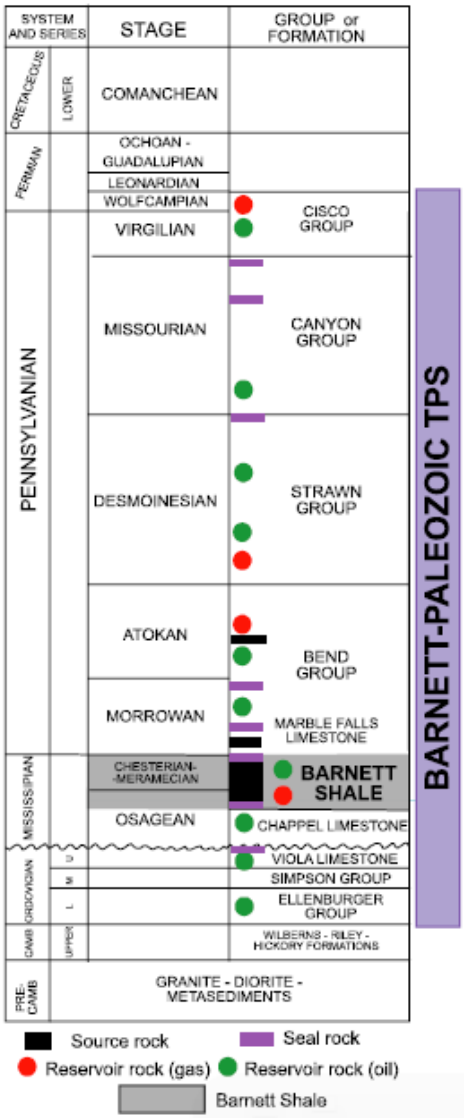

Figure 2. System and series stratigraphic of Fort Worth basin (Modified after Montgomery *et al*. 2005).

Barnett Shale is an unconventional gas reservoir and a source rock for oil and gas. However, production in this area is strongly affected by fractures and karst-related fractures (Bruner and Smosna, 2011). If a fault's trend and orientation were known, one could find and avoid areas that have high rigidity; these could be more fractured in stress

effects. Traditional applications used to determine seismic attributes, such as coherency or curvature attribute, poorly separating tectonic and karst-related faults in the lower Barnett Shale and top Ellenburger Group. In addition, coherency attribute is not sensitive to discontinuities with a finite offset, while curvature attribute is not sensitive to folds and flexures without discontinuities (Marfurt, 2006). Unfortunately, these situations are all found in the lower Barnett Shale and upper Ellenburger Group interface.

2. CONVENTIONAL METHODS IN FAULT DETECTION

2.1 Processing Background

The dataset we used in this project consist of two Harris and Gleason three-dimensional (3D) surveys undertaken in Hamilton County, Texas (Figure 3). Hamilton County is located in the Fort Worth Basin, which is a major petroleum producing geological system. This combined dataset represents approximately 228 square kilometers of 3D data. The data in the Harris 3D survey were acquired in 2006 and consisted of 32453 production shots. The vibroseis source was a non-linear 6-120 Hz sweep with locations spaced 33.5 meters apart. Source lines were separated by a distance of 268 meters. There were 34897 live receivers laid out over a 33.5 meters group interval in the survey. The data of the Gleason 3D survey were acquired in 2005 and consisted of 3627 production shots. This dataset has already been processed. The processing flow is:

- Spherical divergence and geometric spreading.
- Minimum phase conversion.
- Geometry QC/ refraction statics analysis.
- Deconvolution
- Surface consistent gain
- Noise attenuation
- Velocity analysis

- PSTM velocity analysis
- Offset binning
- Kirchhoff ray bending pre-stack time migration
- Residual velocity analysis
- Final stack
- Time variant filter
- FXY deconvolution

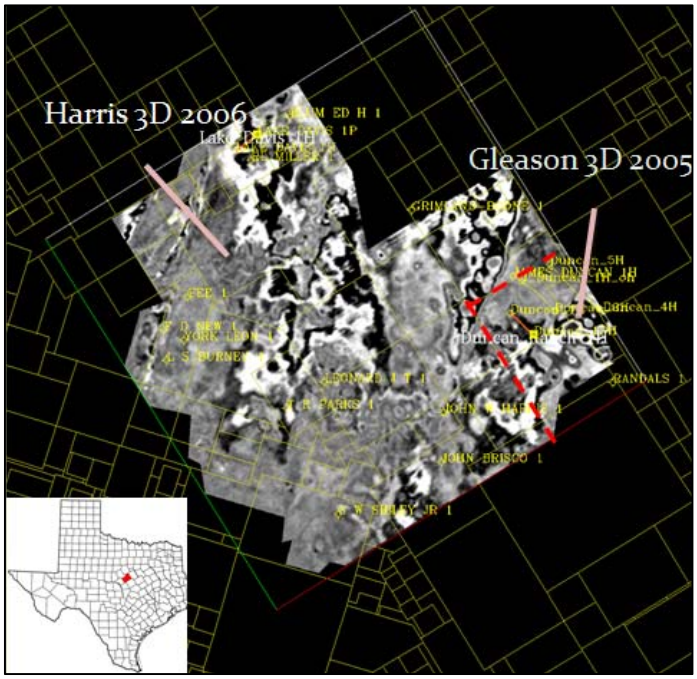

Figure 3. Two 3D Vibroseis surveys merged (Harris 3D in 2006, Gleason 3D in 2005). The time slice shows the irregular boundary of the merged 3D data. The approximate outline of the smaller Gleason 3D survey is shown in dashed red. The total merged survey area is approximately 228 sq. kilometers.

2.2 Seismic Filters

Filters are significant to digital signal processing. In many cases, filters based on a spectrum are important and useful. A spectral filter may be applied to a raw signal's spectrum to get its bandwidth. In time domain, this procedure can be displayed as convolution.

A signal received from a geophone, $x(t)$, normally contains two parts: one is the effective signal, $s(t)$, which reveals underground properties relevant to oil and gas exploration; another one is noise, $n(t)$, which is irrelevant. Thus, by combining these two parts, we can get a real signal:

$$x(t) = s(t) + n(t) \quad (1).$$

One main goal of data processing is to reduce noise and strengthen or maintain the effective signal. Depending on real data processing, the noise spectrum $N(t)$ is very different from the effective signal spectrum $S(t)$. In special situations, the effective signal spectrum is completely separated from the noise spectrum. In such cases, we can design a filter as:

$$H(f) = \begin{cases} 1, when\ S(f) \neq 0 \\ 0, when\ S(f) = 0 \end{cases}. \quad (2).$$

Multiple effective signal spectra may be expressed as:

$$Y(f) = X(f)H(f) \quad (3),$$

where $Y(f)$ is a final result. Because $S(f)H(f) = S(f)$, and $N(f)H(f) = 0$, $Y(f)$ equals $S(f)$. Therefore, noise may be removed after multiplication. In time domain, the relationship between the raw signal and the final result may be expressed as:

$$y(t) = \int_{-\infty}^{+\infty} h(\tau)x(t-\tau)d\tau \quad (4),$$

where $y(t)$ is the filter result and $h(\tau)$ is the filter both in time domain.

In many real signals, however, the noise and effective signal spectra are not completely separated. Depending on the different characteristics of effective signal and noise in the spectrum, we can design different filters to reduce the noise or strengthen the effective signal.

A band-pass filter is a device that passes frequencies within a certain range and rejects frequencies outside that range. The Ormsby filter is one type of band-pass filter, comprised of a filter of trapezoidal shape specified by four corner frequencies, f1, f2, f3, and f4. The filter rejects below f2 and above f3, is linear from f1 to f2 and from f3 to f4, and flat from f2 to f3. A high-pass filter can also be used. The bandwidth of data is 8Hz-120Hz, so the octave of this data is 3.807dB, as calculated by Equation (5), where $f_{high}$is high-frequency, f_{low} is low-frequency:

$$\text{Octave} = \ln\left(f_{high}/f_{low}\right)/\ln 2 \quad (5).$$

Using a band-pass filter, we can extract the high-frequency part and reduce the low-frequency part. High-frequency parts mean short wavelengths, while low-frequency parts mean long wavelengths. Because some large faults have large offsets, which are

much larger than a wavelength, they are found very easily in a seismic map. If the motions of small faults are smaller than a wavelength, however, they are not found easily in a seismic map. For example, Figure 4 shows a cross-line 1157 seismic amplitude map. There are two big reverse faults and one normal fault oriented in a NE-SW direction. A reverse fault is a type of fault, in the Earth's crust across which there has been relative movement, in which rocks of lower stratigraphic position are pushed up and over higher strata. They are often recognized because they place older rocks above younger ones. Reverse faults are the result of compressional forces.

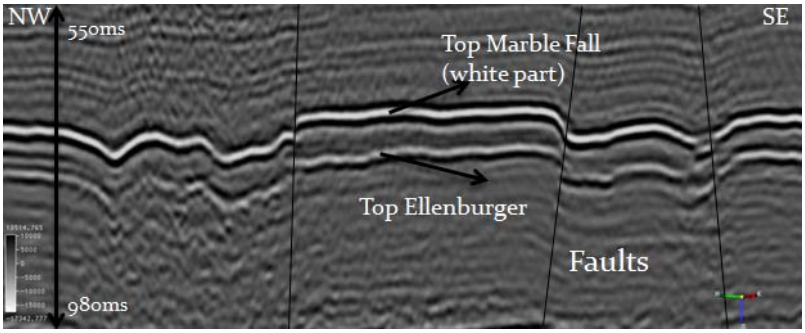

Figure 4. Seismic section amplitude map: cross-line 1157, time range 550-980ms. Two reverse faults are shown.

Using these figures, we can observe high-frequency parts clearly appearing in seismic sections as layers. Some big faults can be easily found by an amplitude map, but for small and medium faults, this method does not detect faults. The results obtained by filtering are one step of the process used to determine seismic attributes.

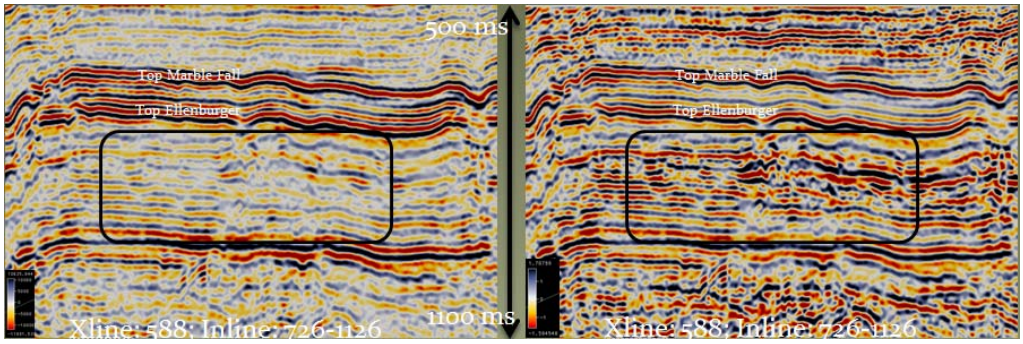

Figure 5. Seismic section: cross-line 558; inline 1126-726; left is whole frequency range (8-120Hz) amplitude map; right is high-frequency part (10-120Hz) amplitude map.

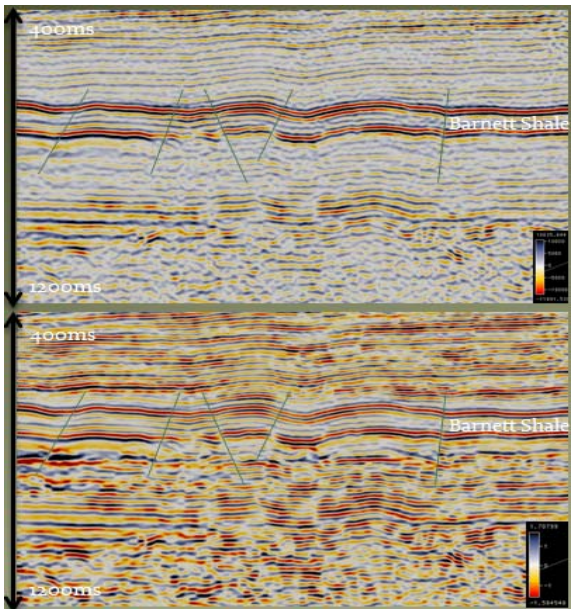

Figure 6. Seismic section in cross-line 800; inline 234-1224: left is whole frequency range (8-120Hz) amplitude map; right is high-frequency part (10-120Hz) amplitude map.

2.3 Coherence Attributes

Using traditional viewing methods such as seismic amplitude maps, it is often difficult to get a clear and unbiased view of faults and stratigraphic features hidden in 3D

data. Although faults are often readily seen on individual vertical seismic cross-sections, many of these cross-sections must be examined to determine the lateral extent of faulting. Stratigraphic changes are difficult to detect on vertical seismic lines because of the limited profile that they present in this view. Time slices are more suitable for detecting and following faults and stratigraphy laterally and are often used for this purpose. Interpretation, however, is often complicated by the fact that time slices can cut through different stratigraphic horizons. This problem can be avoided through the use of the horizon-slice, which is the set of seismic amplitudes associated with an interpreted horizon surface, generally at some consistent stratigraphic level. Other attributes of seismic reflections, besides amplitude, may be calculated and displayed in map view as well, including frequency, phase, dip-magnitude, and dip-azimuth (Bahorich *et al*., 1992). In spite of the fact that horizon-slices and attribute maps are more useful than amplitude time slices for following faults and stratigraphic features, they too have disadvantages. The geoscientist must pick a stratigraphic horizon, which can be difficult and time-consuming (Bahorich and Farmer, 1995).

One of the useful seismic attributes is the coherence attribute, which is effective at interpreting structural discontinuities and stratigraphy features in 3D data. There are three algorithms to measure coherency: crosscorrelation, semblance, and eigenstructure, each based on the continuity of traces in time and depth windows. Input of this attribute requires 3D seismic data. Similar traces are mapped with high-coherence coefficients, whereas dissimilar traces get low-coherence coefficients. The first coherency algorithm based on crosscorrelation was proposed by Bahorich and Farmer in 1995. The second,

introduced by Marfurt *et al*. in 1998, is based on semblance. The third coherency algorithm, introduced by Gersztenkorn and Marfurt in 1999, is based on eigenstructure.

The original crosscorrelation-based coherency algorithm, c_1, provided interpreters with a new way of visualizing faults and stratigraphic features in 3D seismic data volumes. By using relatively simple mathematics to calculate localized waveform similarity in both the in-line and cross-line directions, estimates of 3D seismic coherence may be obtained (Bahorich and Farmer, 1995). In the algorithm, they first crosscorrelate with an in-line trace over a suit of temporal lags, then repeat this process to the target trace with a cross-line trace, and finally calculate the geometric mean of two crosscorrelation values to get the coherence (Figure 7). This process can be expressed as:

$$\mathrm{c}_1(x,y) = [\frac{C_{12}}{(C_{11}C_{22})^{1/2}}\frac{C_{13}}{(C_{11}C_{33})^{1/2}}]^{1/2} \quad (6),$$

where c_1 is the three-trace algorithm and C is the trace.

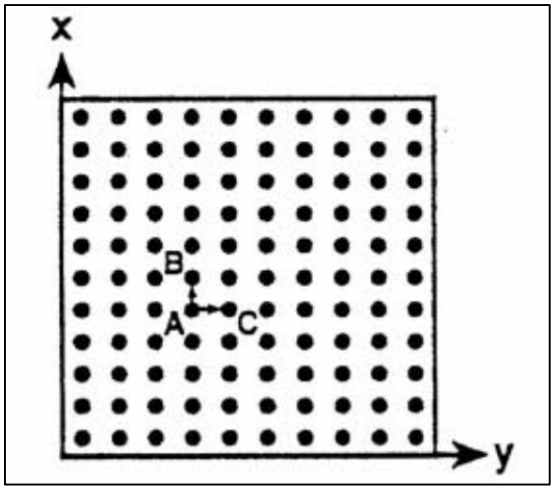

Figure 7. 3D coherence may be measured by calculating seismic trace similarity in the inline and crossline directions; a three-trace operator is depicted. Coherence may be measured from trace A to trace C and from trace A to trace B. A combination of these two-dimensional measurements provides a measure of 3D coherence (Bahorich and Farmer, 1995).

Marfurt *et al*. (1998) and Gersztenkorn and Marfurt (1999) provided coherence attributes based on semblance and eigenstructure, respectively. The c_2 (Marfurt *et al*., 1998) method estimates coherency using a semblance analysis over an arbitrary number of traces. It was generated by calculating the semblance along various dip/azimuth pairs from the covariance matrix. In both the semblance and eigenstructure algorithms, they first estimated dip and azimuth, then calculated either the semblance or a covariance matrix between the target traces. The steps of calculating coherence by the semblance algorithm are: calculating the total input energy, calculating average wavelets within a moving window, estimating coherence traces by their average, and, finally, calculating the energy of average traces. Semblance is defined as the coherency power of traces

divided by the total power of traces. Also, the total power is equal to the coherency power plus incoherency power. This may be expressed as:

$$c_2 = \frac{\sum_{k=-K}^{+K}\left(\frac{1}{J}\sum_{j=1}^{J}[u(k\Delta t - px_j - qy_j)]\right)^2}{\sum_{k=-K}^{+K}\frac{1}{J}\left(\sum_{j=1}^{J}[u(k\Delta t - px_j - qy_j)]^2\right)} \quad (7),$$

where the numerator is the energy of average traces, and the denominator is the energy of all traces.

Subsequently, the c_3 (Gersztenkorn and Marfurt, 1999) eigenstructure method was generated by calculating the eigenvalues of the covariance matrix. The difference between the eigenstructure and semblance methods is that eigenstructure calculates the wavelet that best fits the data, whereas semblance calculates the average wavelet of the data. Marfurt *et al.* (1999) had improved some other coherency algorithms, such as $c_{3.5}$ and $c_{3.6}$, but they are all based on either the semblance method or the eigenvalue method. Both the $c_2$and c_3 algorithms are more sensitive to structural dip. Correlation responds to changes in waveshape only, but semblance responds to both changes in waveshape and amplitude (Marfurt *et al.*, 2000). The eigenstructure of estimate coherence is only sensitive to changes in waveform. In our study, we used the algorithm based on the crosscorrelation method; because Barnett Shale is typical VTI, most layers are horizontal. The results obtained will be discussed and compared in a later chapter. In addition, the coherency estimate has a limitation that several types of geological structures yield similar results. Sometimes, stratigraphic features may be difficult to track, requiring a

tradeoff between analysis windows: if the window increases, better vertical resolution of faults emerges; however, it also smears stratigraphic features. For example:

$$c_3(x, y) = \frac{\lambda_1}{\sum_{j=1}^{j} \lambda_j} \quad (8),$$

where λ_j is the j the eigenvalue of the covariance matrix $\underline{C}$.

2.4 Curvatures

Curvatures are also useful attributes that can be applied in structural and stratigraphic detection. Curvature is a two-dimensional (2D) property of a curve and describes how bent a curve is at a particular point on the curve; that is, how much the curve deviates from a straight line at this point. For a particular point on a curve, its curvature is defined as the rate of change of direction of a curve in mathematics (Roberts, 2001). We can define a 2D line as a parabolic curve of the form:

$$z(x) = a + bx + kx^2 \quad (9).$$

In this equation, k is the curvature coefficient, which is defined as being inversely proportional to the radius of curvature. If we want to define curvature in three dimensions mathematically, we use the least-squares fitting, or some other approximation method, to fit a quadratic surface, $z(x, y)$, from a grid of measurements:

$$z(x, y) = ax^2 + cxy + by^2 + dx + ey + f \quad (10),$$

when the coefficient c in the equation is nonzero, the quadratic surface z is said to be rotated with respect to what mathematicians call the principal axes.

As one kind of seismic attributes, it is sorted into surface second derivative attributes. There are many kinds of curvatures, including most-positive curvature, most-negative curvature, mean curvature, Gaussian curvature. In these curvatures, the most-positive and most-negative curvatures are most useful in structural detection. Figure 8 shows curvature defined in two dimensions as the radius of a circle tangent to a curve.

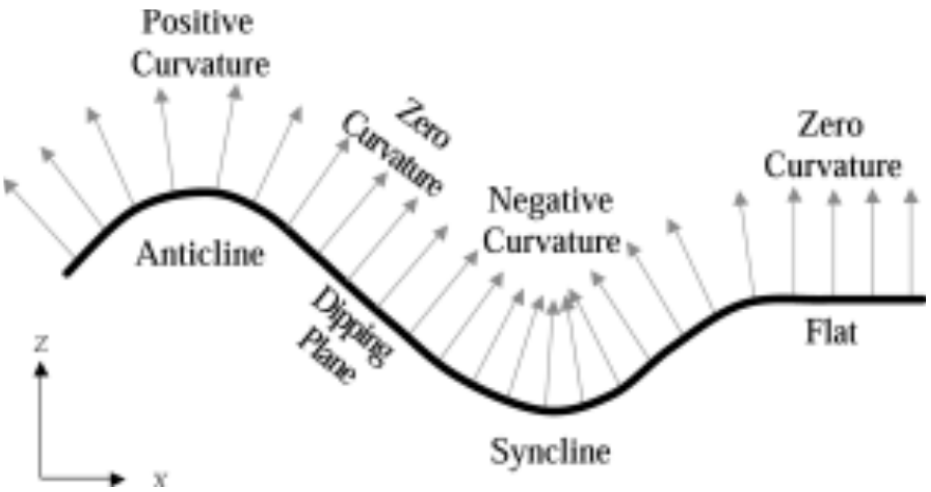

Figure 8. An illustrated definition of 2D curvature; synclinal features have negative curvature, anticlinal features have positive curvature, and planar features have zero curvature (Roberts 2001).

The most-positive curvature and most-negative curvature, k_{pos} and k_{neg} are expressed as:

$$k_{pos} = (a + b) + [(a - b)^2 + c^2]^{\frac{1}{2}} \quad (11);$$

$$k_{neg} = (a + b) - [(a - b)^2 + c^2]^{\frac{1}{2}} \quad (12).$$

Note that the most-positive curvature can be a negative number and the most-negative curvature can be a positive number. Thus, it depends on the shape's features, as shown Figure 9. The definitions of 3D quadratic shapes are expressed as a function of the most-positive curvature k_{pos} and the most-negative curvature k_{neg}. By definition, k_{neg} is less than or equal to k_{pos}. Thus, if both k_{pos} and k_{neg} are less than zero, we have a bowl; if both are greater than zero, we have a dome; and, if both are equal to zero, we have a plane (Marfurt, 2006).

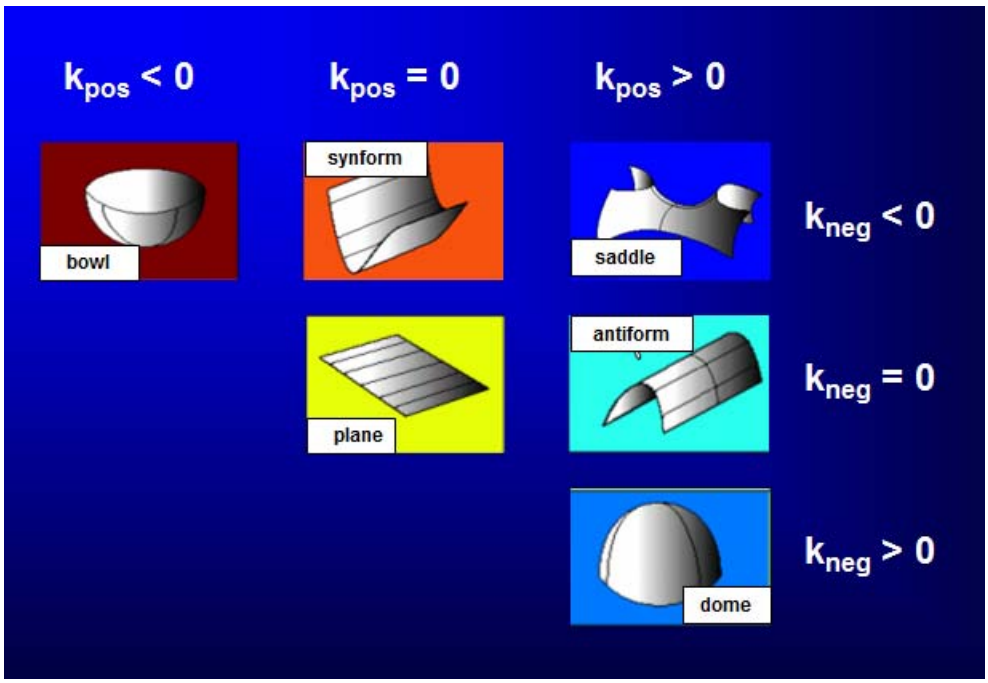

Figure 9. The definition of 3D quadratic shapes, expressed as a function of the most-positive curvature and most-negative curvature (Bergbauer *et al.*, 2003).

Roberts (2001) also goes on to define the mean curvature, k_{mean} , Gaussian curvature, $k_{Gaussian}$, and principal curvatures, k_1 and k_2:

$$k_{mean} = \frac{a(1+e^2)+b(1+d^2)-cde}{(1+e^2+d^2)^{3/2}} \quad (13);$$

$$k_{Gaussian} = \frac{4ab-c^2}{(1+d^2+e^2)^2} \quad (14);$$

$$k_1 = k_{mean} + (k_{mean}{}^2 - k_{Gaussian})^{1/2} \quad (15);$$

$$k_2 = k_{mean} - (k_{mean}{}^2 - k_{Gaussian})^{1/2} \quad (16).$$

Each of the individual curvature attributes gives a slightly different insight into the mapped surface. For example, maximum curvature offers a number of additional benefits over the first derivative-based methods (dip, edge and azimuth), which are commonly used in fault delineation. Curvature contains the added dimension of shape, allowing faults, fault orientations, and faults from other linear surface features to emerge. Comparisons between the dip angle and most negative curvature indicate that curvature can delineate many more surface features, without suffering from the problem of dip saturation. Curvature avoids this problem because it is surface-orientation independent (Roberts, 2001).

Volumetric curvature is a well-established interpretational tool that allows us to image subtle faults, folds, incised channels, differential compaction, and a wide range of other stratigraphic features. The maximum and minimum curvatures define the

eigenvalues of a quadratic surface. By definition, and based on eigenstructure analysis, the maximum curvature is defined as the principal curvature that has the largest absolute.

The wide availability of 3D seismic data permits interpreters to easily find interests and targets. Curvature attribute analysis of surfaces helps interpreters remove the effects of regional dip and emphasizes small-scale features that might be associated with primary depositional features or small-scale faults. The structural geology relationship between curvature and fracture is well established (Lisle, 1994), although the exact relationship between open fractures, paleostructure, and present-day stress is not yet clearly understood. Roberts (2001), Hart *et al*. (2002), Sigismondi *et al.* (2003), Masaferro *et al*. (2003), and others have used seismic measures of reflector curvature to map subtle features and predict fractures. In this study, we primarily use and discuss most-positive curvature and most-negative curvature, which are the most unambiguous of the curvature images for highlighting faults and Karst in the Barnett Shale.

Curvature is a second derivative-based method and is consequently sensitive to any noise contamination which may be present within the surface. This often necessitates the surface to be pre-processed using some form of spatial filter, which can be iterated. The scale of investigation is another important consideration in the computation of curvature. The scale is controlled by the aperture and sampling interval sizes.

2.5 Discussion

Curvature attribute and coherency attribute have different characteristics in structure detection, although their results are similar. These effects are shown in maps

contained in Figure 10. In Figure 10, a) is a fault structure with minimal offset, and stratigraphy is continuous. This fault can be seen on a curvature attribute, because there is dipping change, but it cannot be seen on a coherency attribute because there is no discontinuity in the same event; b) shows a fault with finite offset, which means it has movement in the event, but no dipping change; it can be seen on a coherency attribute, but not on a curvature attribute; c) is an idealized fault which can be seen on both coherency and curvature attributes. If there are folds and flexures, as in d), the attribute indicates sensitivity of folds and flexures; this “fault” will be seen on curvature attribute volumes, but not on coherence attribute volumes. Finally, e) shows attribute sensitivity to infill/collapse features. The deeper part of the fault will be seen on coherence attribute volumes, whereas the shallower part of the fault and the overlying infill will be seen on curvature attribute volumes. Thus, we can say that curvature attribute is more sensitive to dipping change, but coherency attribute is more sensitive to discontinuity.

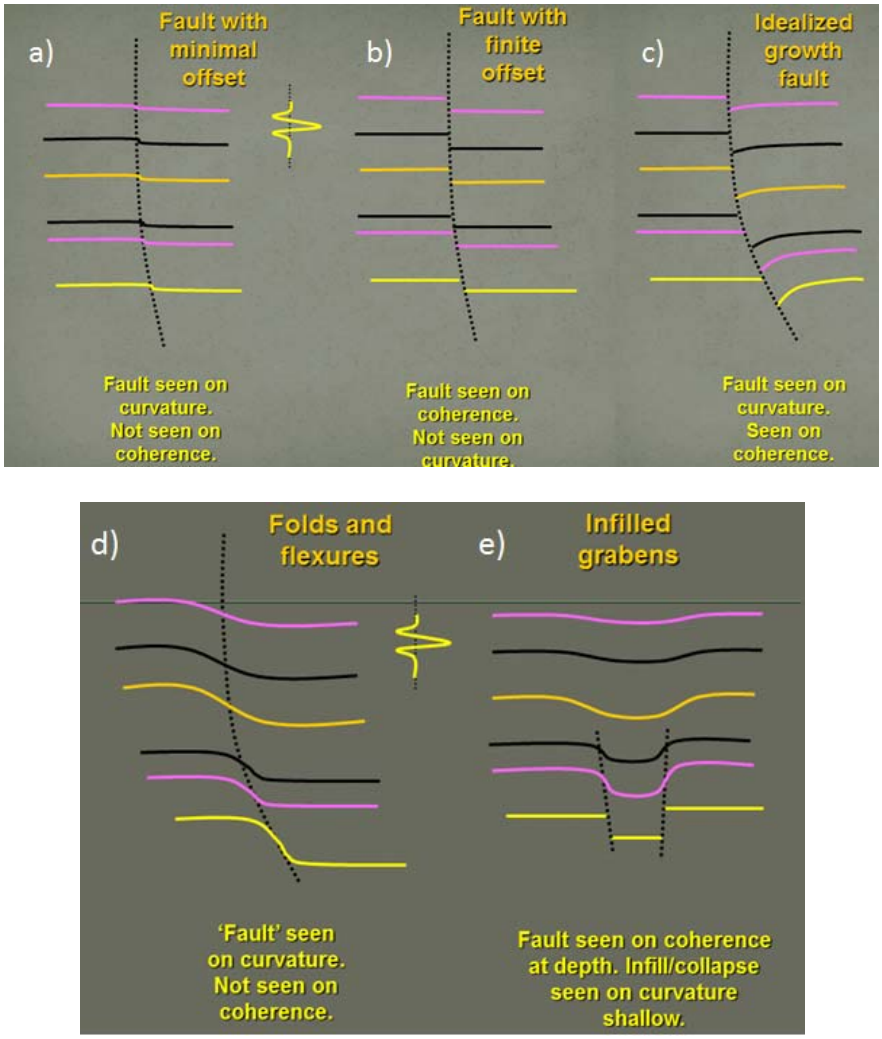

Figure 10. Comparison of characteristics of curvature attribute and coherency attribute: a) idealized fault having an offset much less than one-quarter of the size of the seismic wavelet; b) idealized fault with finite offset and no reflector rotation; c) idealized growth fault, which will be seen on both curvature and on coherency attributes; d) attribute sensitivity to folds and flexures; and, e) attribute sensitivity of infill/collapse features (Marfurt, 2006).

In Barnett Shale fault detection, most large faults can be detected easily in seismic amplitude maps, while small faults cannot be directly found. To illustrate the better features of seismic attributes like coherency attributes and curvature attributes than

normal seismic amplitude map in structure detection. To illustrate the advanced features of seismic attributes over conventional seismic amplitude map, such as coherency attributes and curvature attributes, I will apply these in Barnett Shale 3D data and compare with original data. Figure 11 shows a time slice of the Ellenburger Group at 750ms in Barnett Shale 3D data. The Ellenburger Group is located below the Barnett Shale, which is a water-bearing formation. It consists of clastic fractured limestone and porous dolomite. In Figure 11, a) indicates original seismic amplitude and b) shows the coherency attribute based on the crosscorrelation algorithm. From these two images, fault trends can be easily detected by coherency attribute results indicated by the red and blue arrows; the yellow arrows show sinkholes. Note that the sinkholes can be seen on map b), but not on map a). In addition, the coherency attribute displays better resolution for erosion, shown in the yellow square, whether indicating linear, or other, discontinuities.

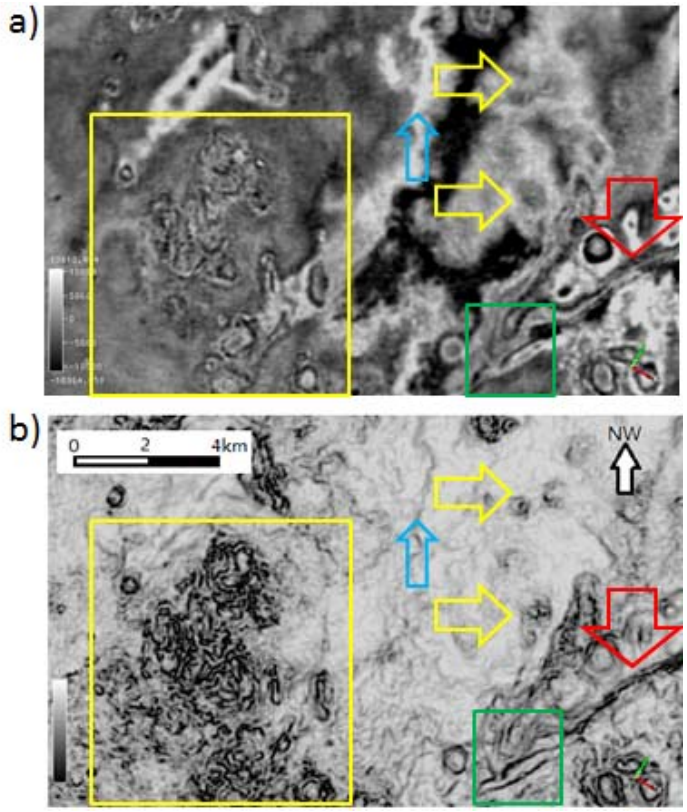

Figure 11. Fault trends: a) original seismic amplitude map; b) coherency attributes map based on the cross correlation method. Red arrows and blue arrows highlight faults, while yellow arrows show sinkholes.

Generally, in our shale reservoir case study, coherency attributes for fault detection, based on either a semblance algorithm or cross-correlation, do not show much discrepancy. The difference between semblance and crosscorrelation is discussed previously: semblance shows better resolution in dipping layers. In Figure 12, map a) is the original seismic amplitude map, while b) and c) are coherency attributes based on crosscorrelation; however, b) is filtered by a high-pass filter (above 10 Hz). On map a), a

big structure, looking like a fault, crosses from north to south. Arrow 1 and arrow 3 point the same fault in map b) and map c), respectively. However, the structure pointed by arrow 2 is smoothed, if compared with the arrow 4 structure. In addition, the arrow 4 anomaly is more correlative than arrow 3, so it could not be a continuous structure connected with the arrow 3 anomaly. We cannot ensure the identification of this anomaly using only coherency attributes; however, we could create more attributes to detect the anomalies.

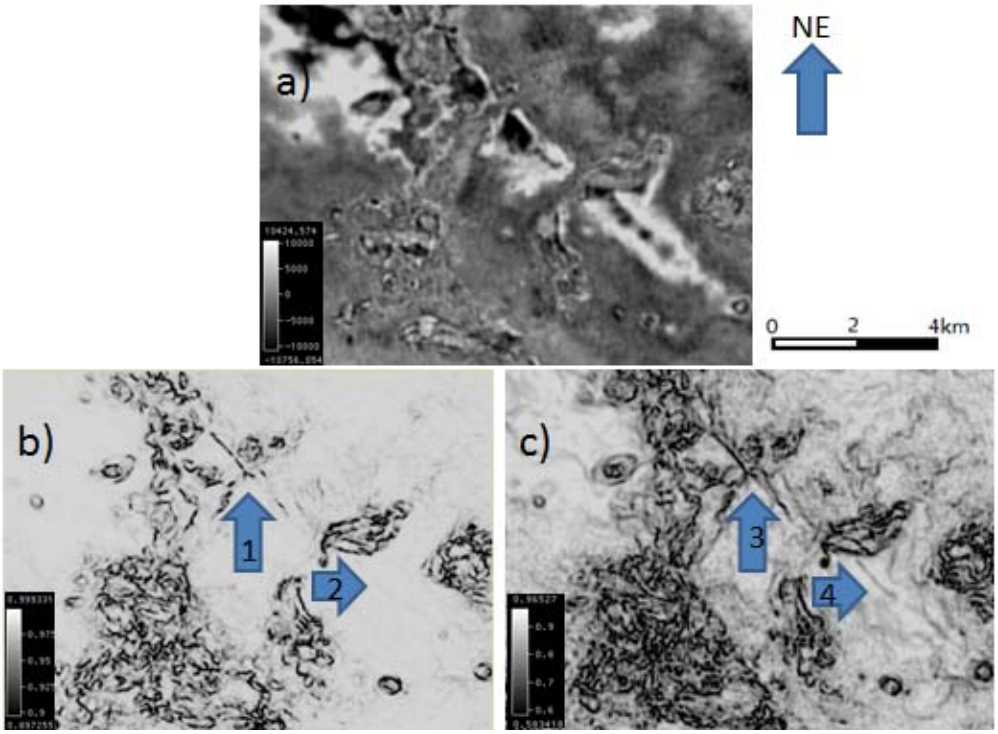

Figure 12. Fault detection: a) original seismic amplitude map; b) filtered by a high-pass filter (greater than 10 Hz); and, c) coherency attributes based on crosscorrelation.

As discussed above, curvature is more affected by noise (Roberts, 2001): because it is closely related to the second derivative of the surface, its quality is very susceptible

to the level of noise contamination. There are often many sources for this noise on a mapped surface, including geological, processing, acquisition, and the horizon autotracking process sources. We applied a high-pass filter (greater than 10 Hz) before calculating curvature attributes, as discussed in chapter 2.1. Figure 13 shows different curvature attribute results in time slice 750 ms: they are most positive curvature, most negative curvature, Gaussian curvature, and mean curvature, respectively.

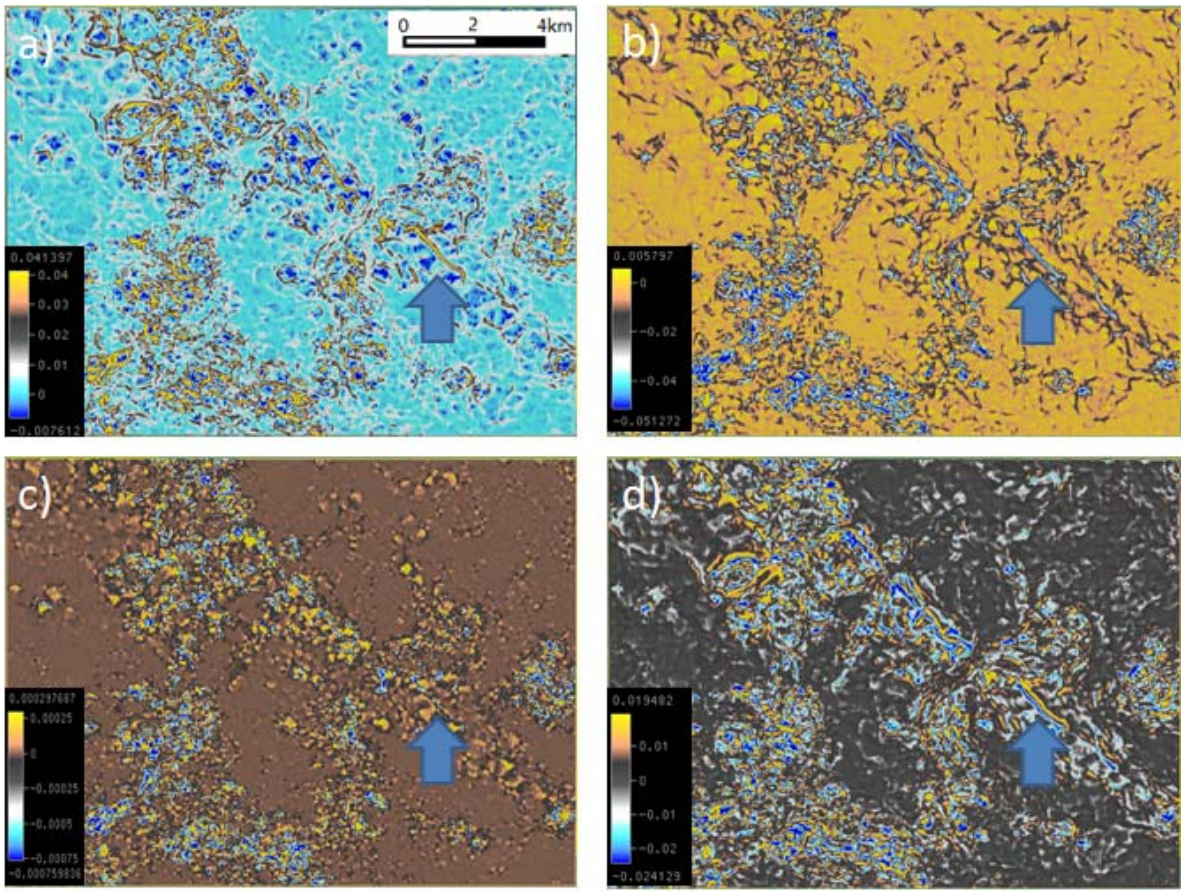

Figure 13. Time slice at 750ms: a) most positive curvature attribute; b) most negative curvature attribute; c) Gaussian curvature attribute; and, d) mean curvature attribute.

Comparing the different curvature attributes shown in Figure 13, there is no significant difference among them, excepting the Gaussian curvature. First of all, we should notice that the color bars are most different, although they have same color. The zero value has a different color in each map. Figure 12 and Figure 13 each display the same 750 ms time slice. The most positive curvature, most negative curvature, and mean curvature attributes successfully delineate the anomaly indicated by the arrow in Figure 13; however, the Gaussian curvature and coherency attributes cannot delineate this anomaly. If looking only at the map of Gaussian curvature, we could not find any meaningful result. The reason provided by Roberts (2001) was that Gaussian curvature is the multiplication of maximum curvature and minimum curvature. If a surface is folded in some way, provided the surface is not broken, stretched or squeezed, then the Gaussian curvature remains constant because these shapes have a zero curvature result in the minimum curvature direction. Therefore, these shapes cannot be differentiated by Gaussian curvature, but require the addition of the mean curvature information. Thus, we can conclude from these time slices that the anomaly in Figure 12, at the surface between the Ellenburger Group and the Barnett Shale, is not a broken structure like a fault, but is caused by surface folding and stretching. In addition, this also indicates why the anomaly disappears from Figure 13: the coherency attribute is not sensitive to folds and flexure (Marfurt, 2006).

For karst structures, coherency attributes have better resolution than curvature attributes (Figure 14). Karst is a geological formation caused by dissolution and fracturing of carbonate rocks, such as limestone or dolomite. The Ellenburger Group

mainly consists of limestone and dolomite: karsting is a complex, large-scale diagenetic event that strongly affected the Ellenburger Group.

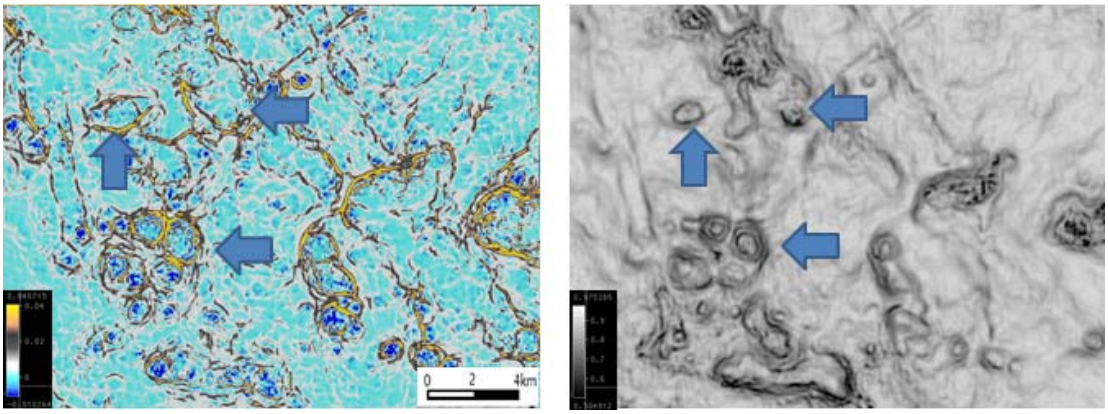

Figure 14. Karst structures: a) most positive curvature attribute; b) coherency attribute based on the cross correlation method. Both slices are at 688 ms.

3. UNCONVENTIONAL ATTRIBUTES

3.1 Fault Attributes Analysis in Structure Detection

As discussed, seismic attributes are sensitive to stratigraphic and structural detection. Coherency attribute and curvature attribute techniques can sometimes highlight their features. However, these methods have some limitations: curvature attributes are more sensitive to folds and flexures, but not sensitive to discontinuities that have a finite offset and no reflector rotation, such as strike-slip faults; coherency attributes are more sensitive to discontinuities, either a finite offset or reflector rotation, but not sensitive to continuous folds and flexures. Thus, we would hope to find an effective way to increase the effects of advantages and reduce the influences of disadvantages. In this chapter, we will make a short introduction and show the better results of this fault attribute.

Tingdahl and Hemstra (2003) have introduced a way to accurately estimate fault orientation from seismic attributes through the use of Principal Component Analysis (PCA). PCA is a standard tool in modern data analysis. It can compress data size and reduce no useful data, and also highlight data similarities and differences. The essence of PCA is that it computes N vectors from a number of observations, where N is the number of variables. The principal components correspond to principal values. PC1 is the principal that has the highest principal value, and the PC2 has the second highest and so forth (Figure 15). The PCs are orthogonal to each other. The first PC is the vector of

maximum variance in the data, and the following PCs are oriented with decreasing variance (Tingdahl and Hemstra , 2003).

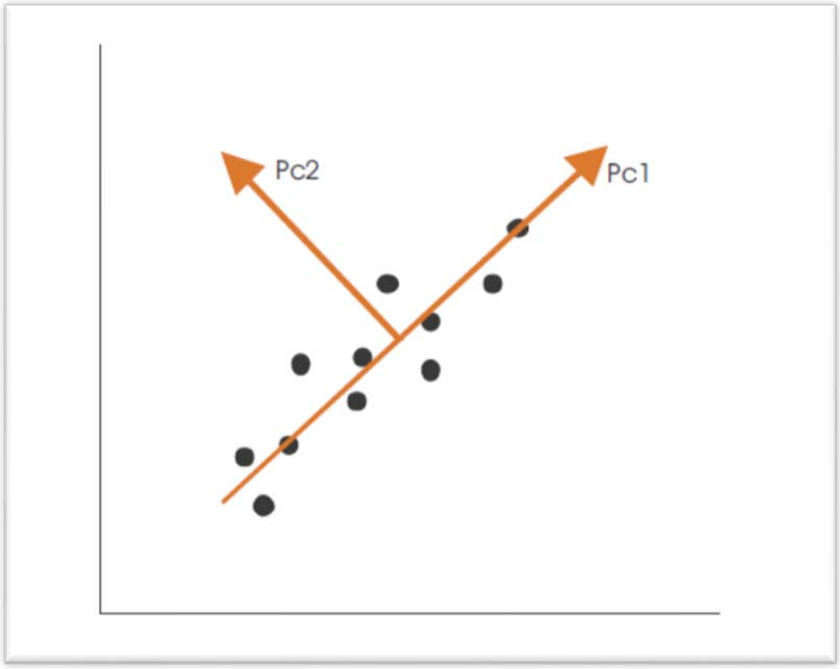

Figure 15. A number of 2D samples form a cigar-shaped point-cloud. PC1 is in the direction of maximum sample variance and PC2 is in the direction of minimum variance. If PCA is computed on a 3D point-cloud, PC1 and PC2 will lie in a plane that fits well to the point-cloud, while PC3 will be the normal to that plane. The plane's dip and azimuth can be computed from that normal (Tingdahl and Hemstra, 2003).

The procedures of in calculating the fault-detection attribute are: 1) spectral decomposition is applied to each trace and trace-to-trace phase discontinuities are determined at a variety of frequencies; 2) a frequency-dependent radial mixing operation (Gulunay and Benjamin, 2008) is applied to improve the signal-to-noise ratio; 3) the filtered frequency bands are wavelet shaped and recombined to produce higher frequency

and higher S/N data; 4) a variety of conventional fault-detection attributes are applied to the recombined data; 5) PCA is applied to all of these attributes to identify lineation; and, 6) the method of Barnes (2006) is used to suppress any remaining events outside of a predetermined range of orientations.

Using spectral decomposition, we can obtain phase information at isofrequency. Partyka *et al*. (1999) pointed out that phase at specific frequencies resulted in particularly clear fault images on time slices. Because phase is sensitive to subtle perturbations in the seismic character, it is ideal for detecting lateral acoustic discontinuities. Spectral decomposition methods may not only be used to compensate for fault-detection attributes in this study; other functions will be discussed in a subsequent chapter. I have talked about subcube data, and create seismic attributes.

The PCA may be calculated by the Singular Value Decomposition (SVD) method and application of a fan-filter, dash-line filter, and fault-shape filter. Use of the SVD method as one way to generate PCA was introduced by Shlens (2009). It reveals single underlying structures in complex data sets using analytical solutions from linear algebra. The primary motivation is to decorrelate the different seismic attributes and remove second order dependencies. In mathematics, PCA can be summarized as: organize data as an m*n matrix, where m is the number of measurement types and n is the number of samples; subtract off the mean for each measurement type; and, calculate the SVD or the eigenvectors of the covariance (Shlens, 2009).

The fan-filtering method has been used for many decades. Treitel *et al.* (1967) first showed the utility of both the fan-pass filter algorithm and fan-reject filter algorithm. They found a 2D time-space domain operator that passes events recorded from a given in-line seismic array, whose apparent velocities fall within a range, by specifying the required transfer function in the (f , k) plane, where f and k are the temporal and spatial frequencies, respectively. In addition, Barnes (2006) showed a discontinuity filter that only passes discontinuities to highlight faults for seismic data interpretation. The discontinuity filter, based on a fan-filter, improves and highlights seismic discontinuity attributes for fault detection. They created discontinuity attributes and applied the discontinuity filter to get fault attributes. In this study, we apply Barnes's method and improve its procedures to create new fault attributes by SVD and filters.

This new procedure of determining fault attributes shows better resolution in revealing faults, karst, and other structures. Faults and karst are very important factors to the study of Barnett Shale gas reservoirs and Ellenburger Group source rocks and oil reservoirs. This is primarily because oil and gas can transfer between faults and fractures, while water can transfer from Ellenburger water formations. Bruner and Smosna (2011) suggested that production wells that encounter faults and karst tend to be less productive in Barnett Shale because faults and karst serve as transferal mechanisms that take water from the Ellenburger Group to the Barnett Shale, releasing trapped gas. Figure 16 shows the subcube data set of Harris and Gleason 3D surveys from Hamilton County, Texas. The parameters are time from 400 ms to 1200 ms, cross-line from 600 to 900, and inline

from 750 to 1150. The figure shows a time slice at 750 ms, which is the interface between the Ellenburger Group and the Barnett Shale.

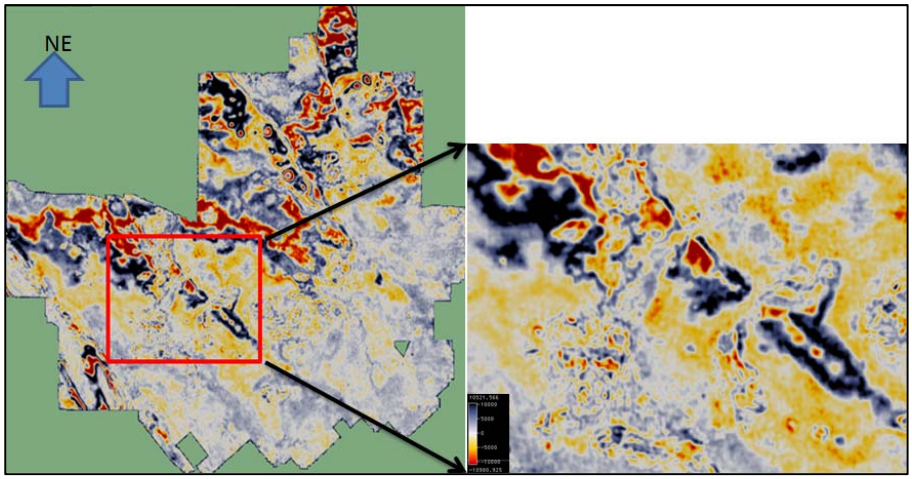

Figure 16. The time section at 750 ms: subcube data showing a main fault cross this area; the inset at left reveals that it is not shown very well.

This dataset was high-quality processed by Geokinetics in 2006, using deconvolution and noise attenuation techniques. Using the spectral decomposition method to get a phase map, we first applied a band-pass filter (3Hz - 10Hz) to establish the low-frequency portion. We then performed trace mixing to smooth the low-frequency portion and then multiple with high-frequency part; using high-frequency part to make coherency attribute, curvature attribute and variance attribute (Figure 17).

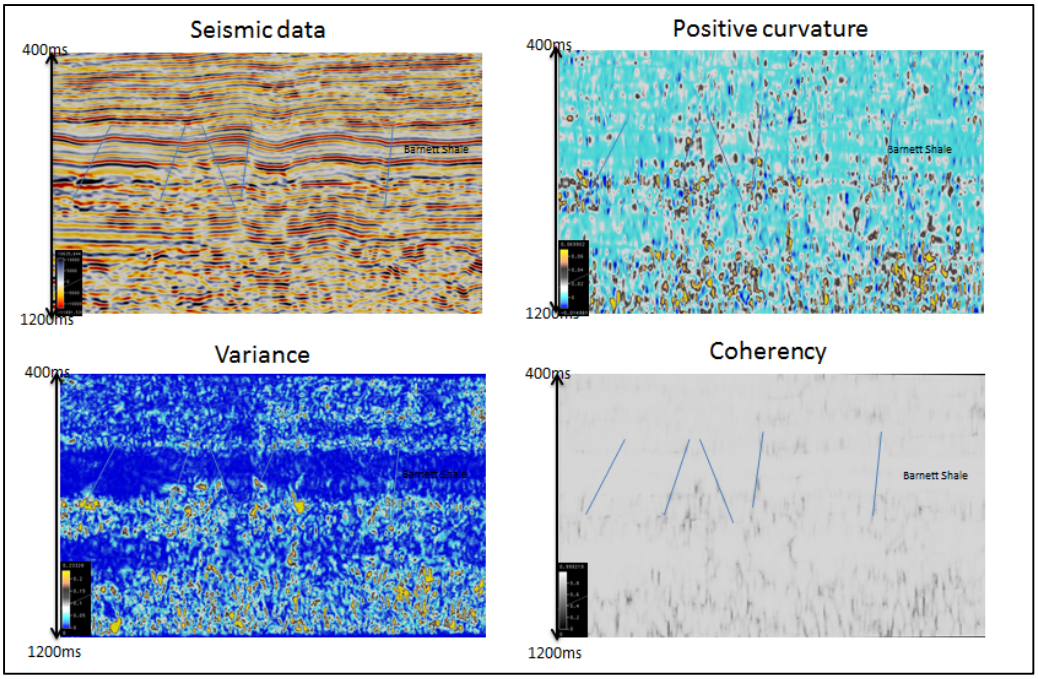

Figure 17. Section views from 400ms to 1200ms: a) seismic data high-frequency portion, 10Hz to 120Hz; b) positive curvature attribute; c) variance attribute; and, d) coherency attribute.

These attributes were processed with little noise effect. Anomalies are caused by different structures, layers, folds, and flexures. All these attributes are sensitive to faults. It is possible to obtain PCA using the SVD method to highlight these anomalies and reduce undesired results. In Figure 18, map a) is the section view of PCA results and b) plots the application of fault-filter (fan-filter, dash-line filter, fault-shape filter) in our PCA results. Figure 19 and Figure 20 show another attribute comparison in fault chimney detection. These fault chimneys in found in the low Barnett Shale and top Ellenburger Group are actually caused by karst-related fractures; these appear as cylindrical shapes in

a time slice (Figure 21). Our fault attribute can display fault separation, unlike other attributes.

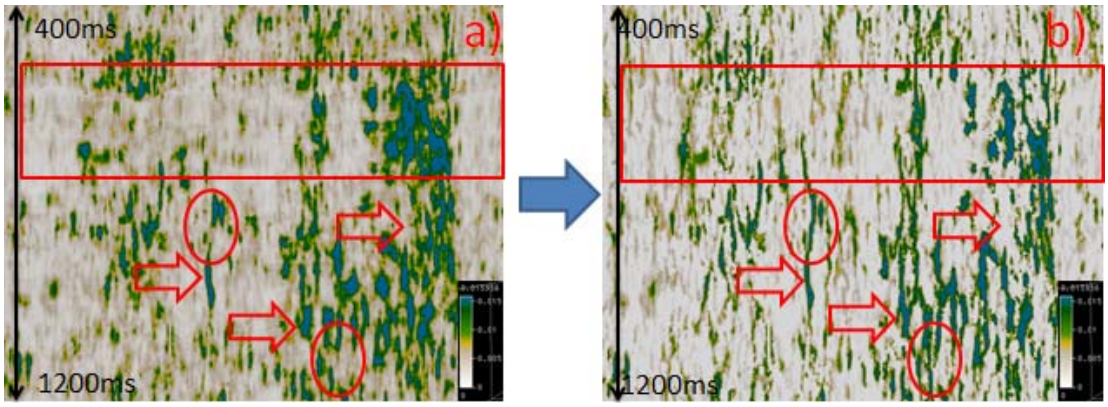

Figure 18. PCA results: a) section view; and, b) the application of fault-filter to PCA results.

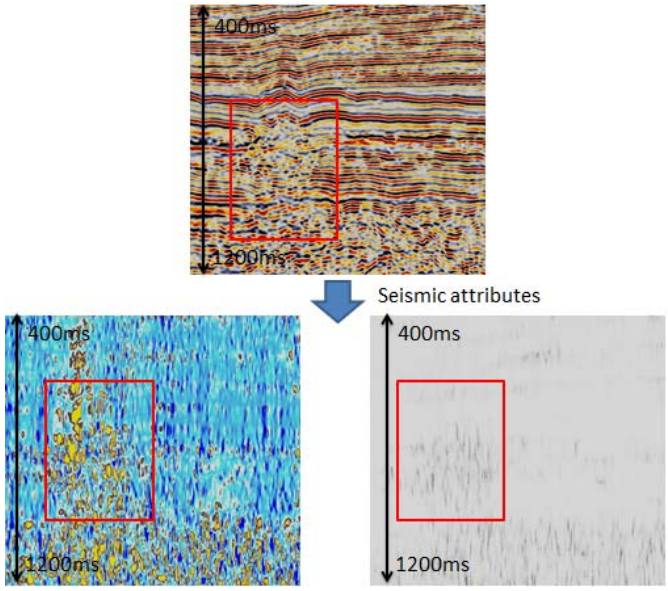

Figure 19. Fault chimney detection; Positive curvature attribute and coherency attribute.

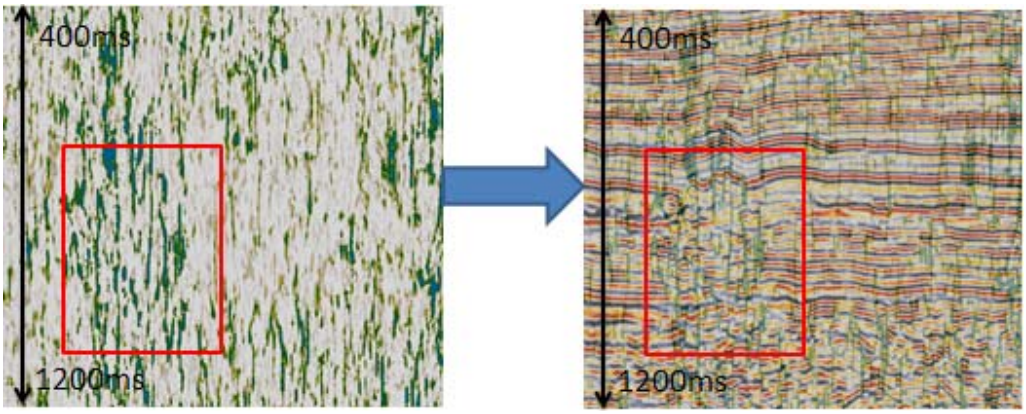

Figure 20. Fault chimney detection: a) fault attribute; b) fault attribute merged into original data.

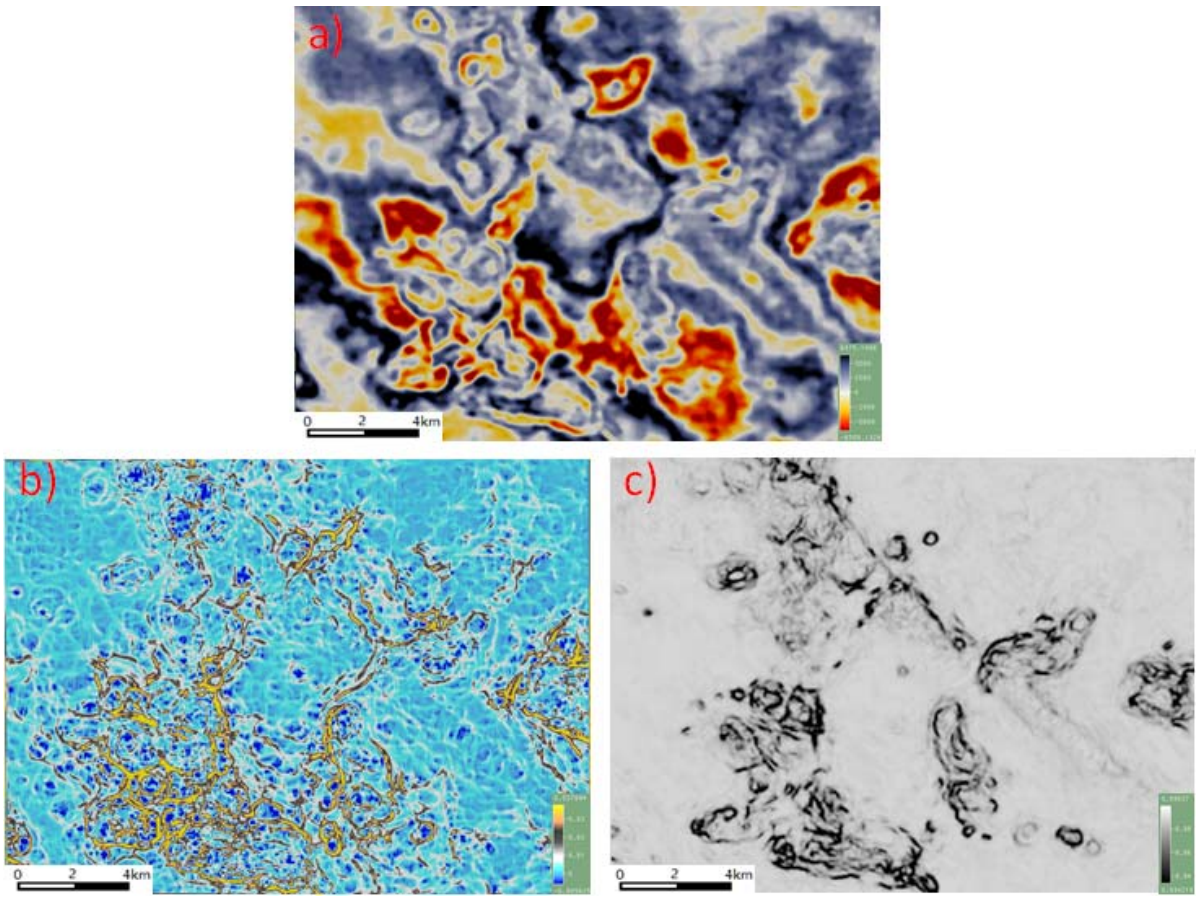

Figure 21. Time slice views in 718 ms: a) original seismic data; b) positive curvature attribute; and, c) coherency attribute.

Figure 21 and Figure 22 display a comparison of the fault attribute and other attributes in a time slice view. The fault attribute can show fault trends (the red line in figure) and Karst (red arrows in Figure 22) like the coherency attribute, which cannot be shown clearly in the curvature attribute; in addition, the fault attribute can delineate interface folds and flexures (blue arrows in figure 22) like the curvature attributes, which cannot be delineated in the coherency attribute.

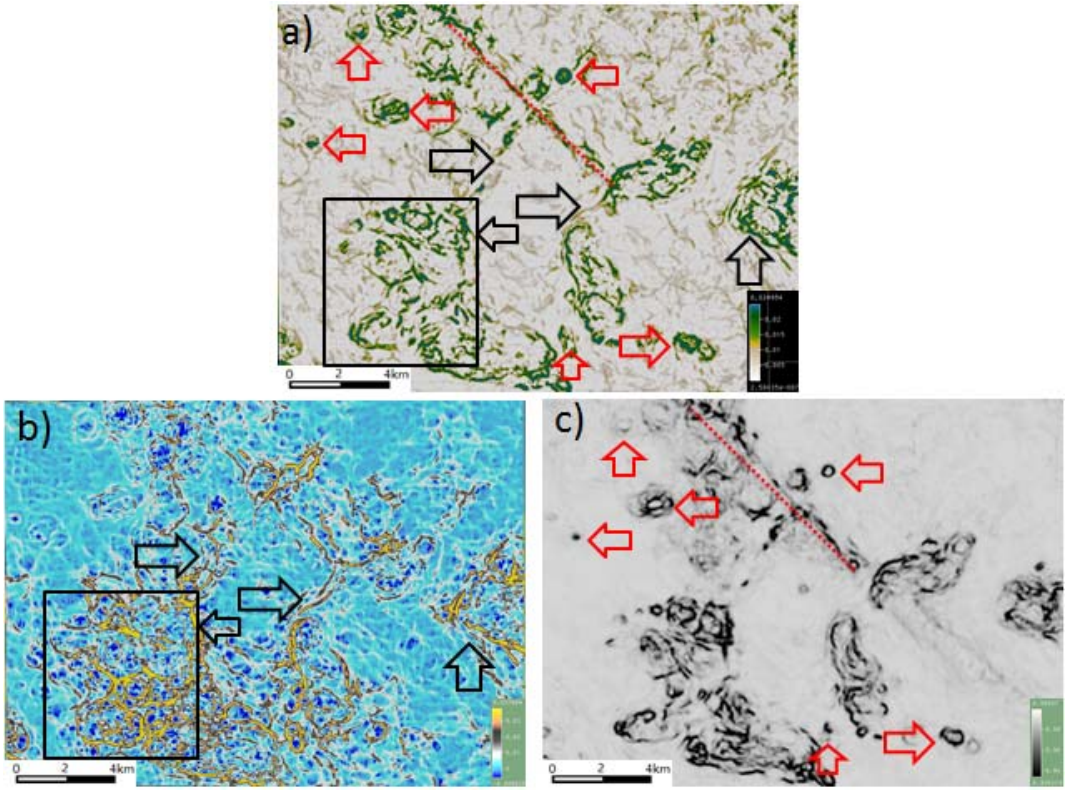

Figure 22. Attribute comparison: a) time slice of the PCA fault attribute at 750ms; b) positive curvature attribute; and, c) coherency attribute based on cross correlation method. In the fault attribute map, red arrows point the Karst and red dashed line shows a fault trend; the black arrows and black square point to minor faults not seen on the coherency attribute. Note that the PCA

attribute is less noisy than the curvature attribute, but shows more features than the coherency attribute.

Therefore, seismic attributes, particularly fault attribute, provide a good understanding of faults and karst structures. To increase prospecting efficiency and production, water formations and paleo-reservoirs are avoided. In Figure 23, the yellow line indicates the horizon of interface between the Barnett Shale and Ellenburger Group. The blue arrows show a fault crossing from north to south. The red arrows indicate surface folds and flexures. The color bar indicates high-value highly curved lines in karst structures; these curved lines are quite vertical.

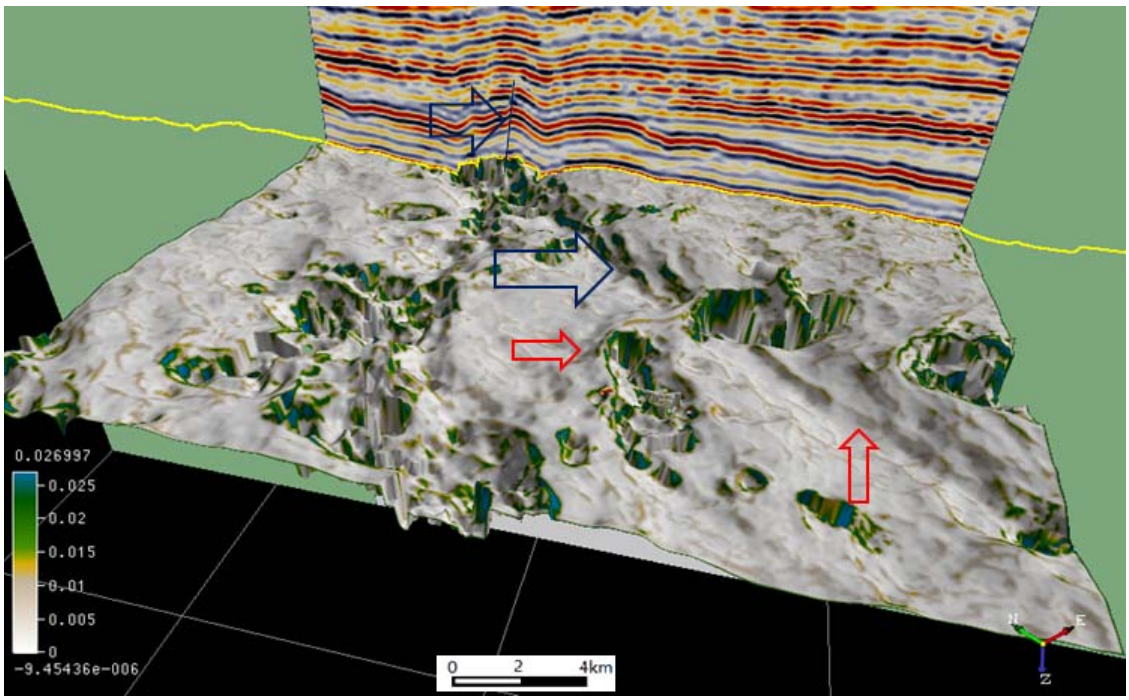

Figure 23. Fault attribute merged into the horizon of interface between the Barnett Shale and Ellenburger Group.

These results compare well to coherency attributes. Some low-value results are similar to curvature attributes, which delineate folds and flexures. It is, therefore, possible to separate different curvatures of surfaces and similarities using the fault attribute method, which cannot be found using coherency attribute or curvature attribute approaches.

3.2 Spectral Methods in Structure and Lithology Detection

Spectral decomposition is a good way to show how lithologies change with different frequencies. By transforming a seismic dataset from a time domain into a frequency domain using spectral decomposition, structural and stratigraphic delineation, such as channel sands and structural settings involving complex fault systems, can be better indicated. The amplitude spectra show temporal bed thickness variability, while the phase spectra delineate lateral geologic discontinuities. Spectral decomposition of a reflection seismogram was introduced as a seismic interpretation technique by Partyka *et al*. (1999). They noted that phase at specific frequencies resulted in particularly clear fault images on time slices. They also recognized that seismic frequency spectra using short windows were greatly affected by local reflectivity spectra, and, thus, carried information about layer characteristics. They further showed that simple layers of certain thicknesses exhibit notched spectra and that the pattern of frequencies at which these notches occur sometimes can be used to infer layer thickness. They finally observed that, for this reason, seismic images at different frequencies preferentially illuminate, or

respond to, geological variations differently. Spectral time-frequency analysis has since become an important practical seismic interpretation tool that has widespread use. Chakraborty and Okaya (1995) introduced the short-time Fourier transform (STFT) in earlier spectral decomposition work. This method is equivalent to the crosscorrelation of a seismic trace with a sinusoidal basis over a moving time window. They also developed the continuous wavelet transform (CWT) approach, which is the crosscorrelation of the seismic trace against a wavelet dictionary. Finally, they developed the matching pursuit decomposition (MPD) technique, which is the decomposition of the seismic trace into basis atoms. In addition, Puryear *et al.* (2012) demonstrated the application of constrained least squares spectral decomposition, which is an inversion-based algorithm for computing the time frequency analysis, formulated and applied to modeled seismic waveforms and real seismic data. In our study, we mainly compare Discrete Fourier Transform (DFT), CWT, and CLSSA in structure lithology detection.

DFT is the mathematical basis of the Fourier transform used in spectral decomposition. This method, however, has limited vertical resolution because the seismogram must be windowed. The spectral energy is distributed in time over the length of the window, thereby limiting resolution (Castagna *et al.*, 2003). The Fourier transform projects infinite sinusoidal bases on the signal and is thus the LMSE solution for the Fourier series coefficients:

$$G(f) = \int_{-\infty}^{+\infty} g(t)e^{-i\omega t}dt \qquad (17),$$

where t is time, f is frequency, ω is $2\pi f$, $g(t)$ is the continuous time signal, and $G(f)$ is the continuous complex spectrum. The DFT is a modification of the Fourier transform for application to discrete signals. In computing the DFT, the sinusoidal basis functions are only orthogonal when their periods are integer fractions of the period of the lowest non-zero frequency. The DFT is defined as follows:

$$G(k\Delta f) = \sum_{n=0}^{N-1} g(n\Delta t) e^{-\frac{2\pi i}{N} k\Delta f n\Delta t} \quad , \; k = 0, \dots, N-1, \qquad (18),$$

where N is the number of samples, n is the time sample index, Δt is the time increment, k is the frequency sample index, Δf is the frequency increment, $g(n\Delta t)$ is the discretely-sampled time signal, and $G(k\Delta f)$ is the discretely-sampled complex spectrum. The STFT is the DFT applied as a function of time using a sliding time window, which is usually tapered to have a desired transfer function. This amounts to cross-correlation of the orthogonal sinusoidal basis functions with a windowed segment of the signal. The time-time panelg_ω is first derived from the windowed signal and expressed as a function of window center and window sample:

$$g_\omega(n\Delta t, m\Delta t) = w(m\Delta t) g\big((n+m)\Delta t\big) \qquad (19),$$

$$n = 0, \dots, N-1 \; and \; m = -\frac{M-1}{2}, \dots, (M-1)/2$$

where n is analysis time sample (center of the window), m is the window sample index, M is the number of samples in the window, $w(m\Delta t)$ is the window function (usually tapered towards zero at the endpoints in order to minimize the Gibbs Effect), and

$g_\omega(n\Delta t, m\Delta t)$ is the windowed time-time panel as a function of window position and window sample. Second, the forward STFT is defined as the DFT of a time-time panel over the dimension of the window sample model. This results in a time-frequency panel:

$$G(n\Delta t, k\Delta f) = \sum_{m=-(M-1)/2}^{(M-1)/2} g_\omega(n\Delta t, m\Delta t) e^{-\frac{2\pi i}{M} k\Delta f m\Delta t} \quad (20).$$

The CWT technique applies a narrow-band filter to the signal in the time domain using a stretched version of a mother wavelet; it decomposes the seismic data into octave or sub-octave scales of the original data. For seismic applications, the semi-orthogonal Morlet wavelet is commonly preferred. The forward CWT for a real wavelet dictionary is as follows:

$$W(a,b) = \frac{1}{\sqrt{a}} \int \psi\left(\frac{t-b}{a}\right) s(t) dt \quad (21),$$

where a a scaling parameter; b is a translation parameter, ψ is the mother wavelet, $s(t)$ is the signal, and $W(a,b)$ is the CWT scale decomposition.

Puryear *et al*. (2012) introduced this new method of spectral decomposition. They inverted the normal equations by applying an iteratively re-weighted least squares regularization algorithm to the complex spectral decomposition inverse problem using a minimum support functional, as defined by Last and Kubik (1983) and Portniaguine and Zhdanov (1998). The detailed algorithm was described by Puryear *et al.* (2012). They introduced diagonal matrices W_m and W_d, which are model and data weights. The initial model weighting matrix on the first iteration is:

$$W_m = I \tag{22}$$

W_d remains constant throughout the iterations. For a Hann taper, we use:

$$W_d = Diag\left(0.5 + \cos\left(\frac{2\pi n \Delta t}{l}\right)\right) abs(d_0) \tag{23}$$

The weighted quantities are:

$$m_w = W_m{}^{-1} m \tag{24}$$

In order to solve this equation, they applied Tilhonov regularization (Tikhonov and Arsenin, 1977) and replaced it with a well-posed minimization problem (Portniaguine and Zhdanov, 1998). The model parameters are reconstructed using the following formula:

$$m = W_m m_w \tag{25}$$

If more compact spectra are desired, as would be the case for known sparse spectra, or simply to sharpen frequency peaks for attribute analysis, additional iterations can be performed. The model weights are updated by applying the following:

$$W_m = Diag\big(abs(m)\big) \tag{26}$$

Puryear *et al*. (2012) proposed that the CLSSA approach has better temporal and frequency resolution than either the CWT or DFT methods. They applied CLSSA to a seismic data set containing a turbidite channel system. We applied these methods to the Barnett Shale data set and compared the use of CLSSA, CWT, and DFT to detect faults.

The Barnett Shale 3D data set covers approximately 228 square kilometers. The vibroseis source is a non-linear 6-120 Hz sweep. The dominant frequency of the 3D data set is about 45 Hz (Figure 24). The trace in the figure is located at xline 738, inline 565; the frequency range is about 10-100 Hz.

After applying this trace to spectral decomposition methods, we can display the results in time-frequency panels. Figure 25 shows a time-frequency panel with DFT, CWT, and CLSSA methods. The Hann-windowed CLSSA result used a 40 ms window. In map a), the time-frequency panel is correlated with the trace; the y-label is time, which is same as the trace; x-label is frequency range. In map b), the first panel is the DFT result, and the second is the CWT result; the red color means high-spectral amplitude. Comparing map a) and b), we observe that the CLSSA amplitude in the frequency range is much narrower than the DFT amplitude. We propose that this result was obtained because DFT is based on the Fourier theory, which is more affected by windows. CLSSA, however, is an inverse-based method; it has reduced the influence of windows. We will show more cases about windows effects and side-lobe effects in the late work. Using Figure 25, we conclude that spectral amplitude, which is caused by different reflection coefficients, can be highlighted in different frequency domains, indicated by the yellow dashed line and green arrows in map a). Spectral decomposition can be used to detect different interfaces caused by lithology changes in different frequency results.

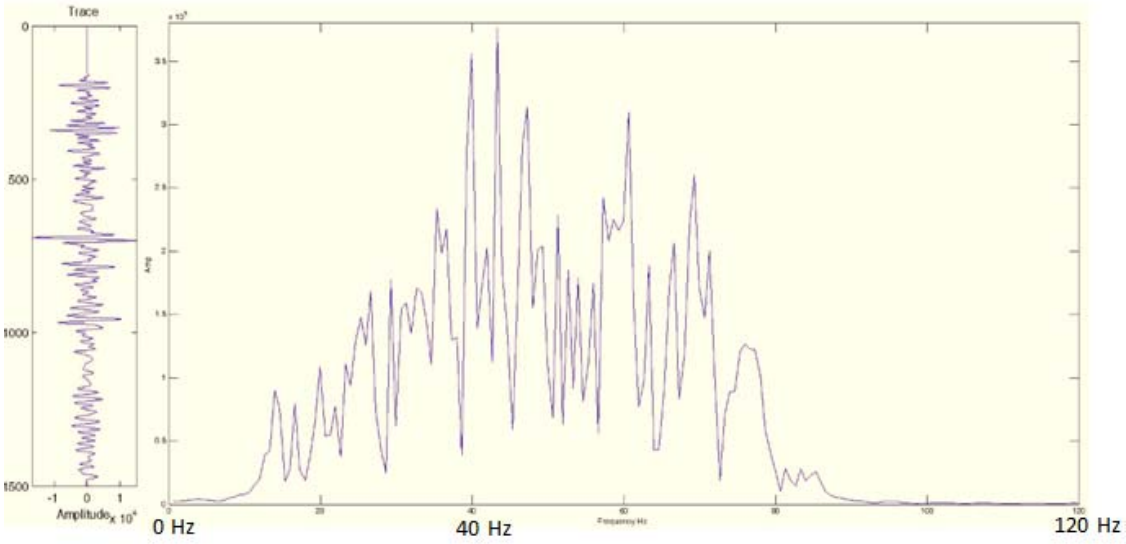

Figure 24. The trace at xline 738, inline 565, and its spectrum.

We then applied these methods to all 3D data set images that suggested the presence of many faults. In the original data map view, some large faults can be directly observed, but the data must be well-processed before interpretation. In Figure 26, three faults can be found in a seismic section view; the time range of depth is about 550 ms to 980 ms. In the map at left, a chimney caused by faults appears; however, it is not possible to distinguish these faults using the original seismic data. Figure 27 shows the amplitude and phase spectrum of the CLSSA results. Map a) shows the 40 Hz amplitude (upper) and phase spectrum (lower) of the CLSSA result, using a 20 ms Hann-window; map b) shows the 25 Hz amplitude (upper) and phase spectrum (lower) of the CLSSA result, using a 20 ms Hann-window. The red color in the amplitude figure indicates the highest spectral amplitude that correlates with the high-reflection coefficient interface between the Marble Falls Limestone and Barnett Shale. In reviewing both 40 Hz and 25 Hz results, two more faults, indicated by white arrows, appear using the amplitude and phase

spectrum. These did not appear on the original seismic data. These improvements can be also seen using the DFT results, obtained using a 20 ms Hann-window. Map a) shows the 25 Hz amplitude (upper) and phase spectrum (lower) of the DFT result; map b) shows the 40 Hz amplitude (upper) and phase spectrum (lower) of the DFT result.

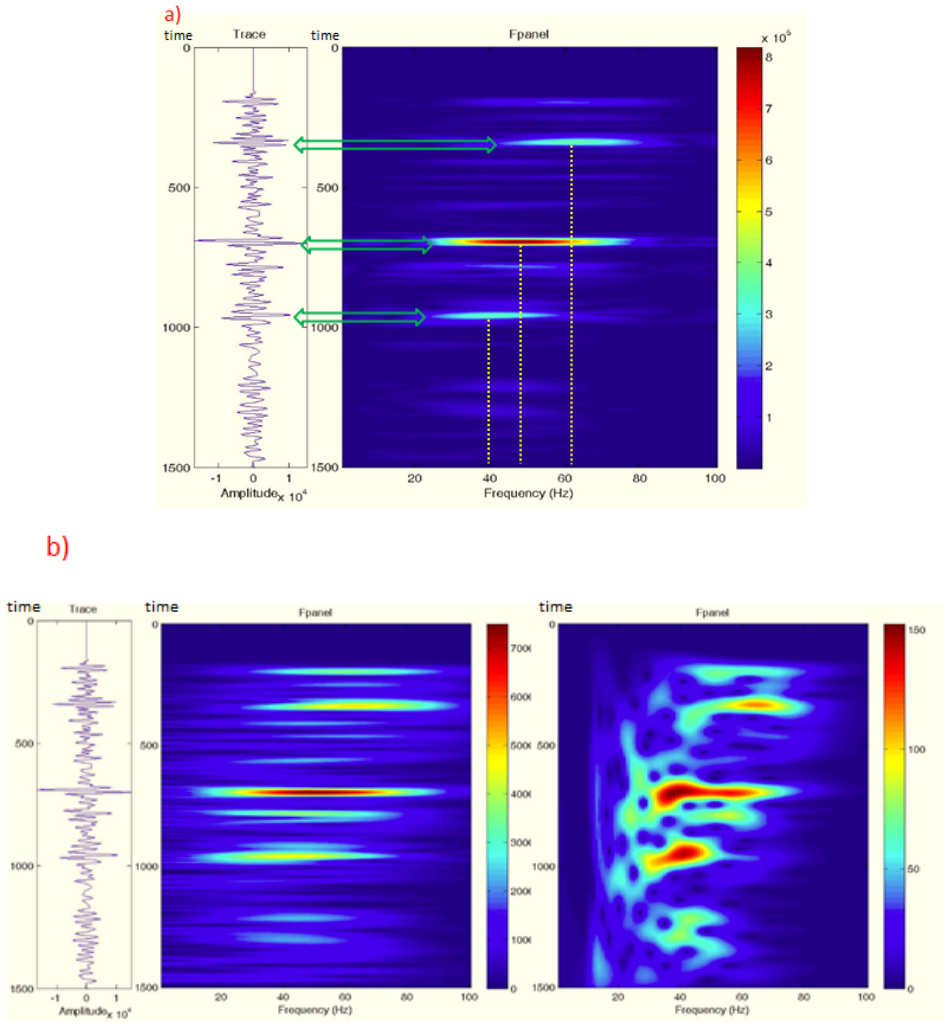

Figure 25. Time frequency panels: a) CLSSA result, calculated by a 20 ms Hann-window; b) DFT and CWT results; the DFT result was calculated by a 20 ms Hann-window.

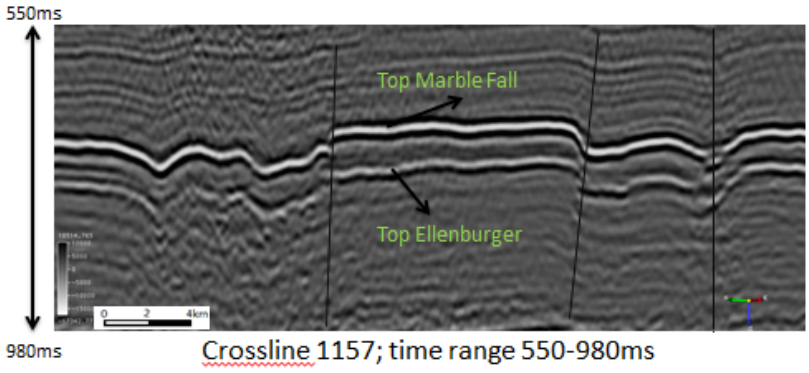

Figure 26. Section view of original data showing three faults trends.

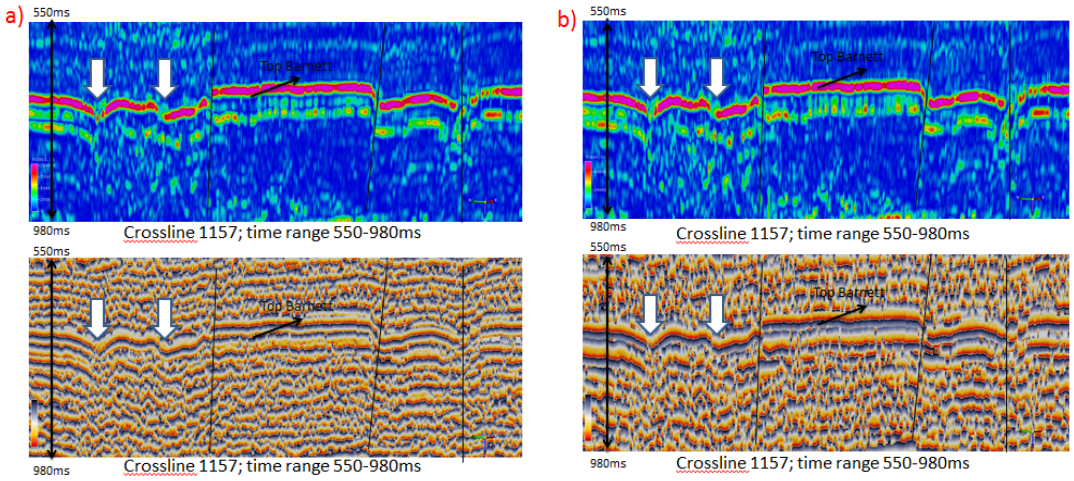

Figure 27. CLSSA result using 20 ms Hann-window: a) 40 Hz amplitude (upper) and phase spectrum (lower); b) 25 Hz amplitude (upper) and phase spectrum (lower).

We observe that spectral decomposition can highlight more discontinuities than the original seismic data. From both the CLSSA and DFT results, we can also observe that the top Marble Falls Group is more continuous than the top Ellenburger Group, which is also not evident in the original data. These discontinuities are caused by diagenesis in the Ellenburger Group, and produce an unconformity: extensive cave systems formed at a composite unconformity, which was associated with karsting

dissolution that lasted several million years to several tens of million years (Loucks et al., 2007).

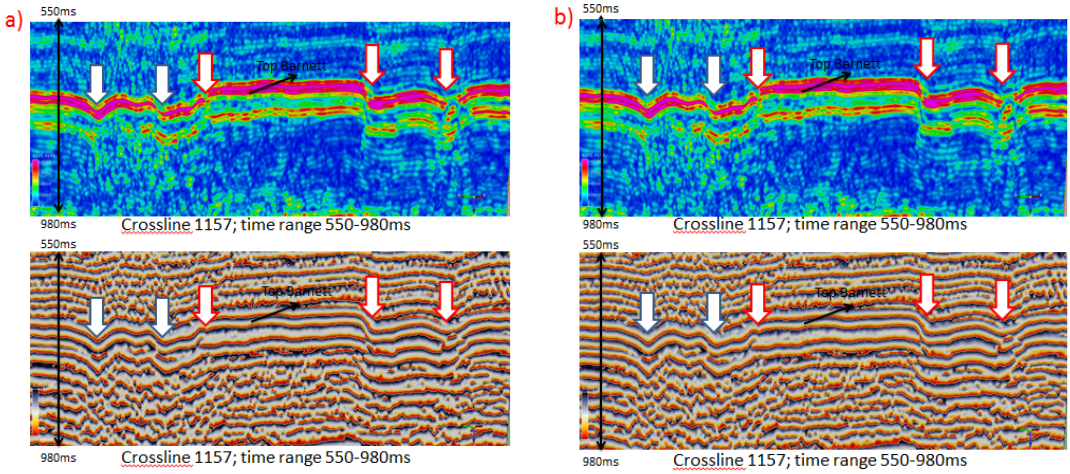

Figure 28. DFT result using 20 ms Hann-window: a) 25 Hz amplitude (upper) and phase spectrum (lower); b) 40 Hz amplitude (upper) and phase spectrum (lower).

Comparing the section views of CLSSA and DFT in the same window, CLSSA results show better resolution for fault detection, as indicated by the white arrows in Figure 27 and Figure 28. Events are much narrower in the CLSSA results because the CLSSA method reduces the effects of window side-lobes. Using this advantage, spectral decomposition methods can also divide different layers that cannot be separated in the original seismic data (Figure 29). In a time slice view, the CLSSA technique is effective at detecting discontinuity features like fault attributes and other seismic attributes.

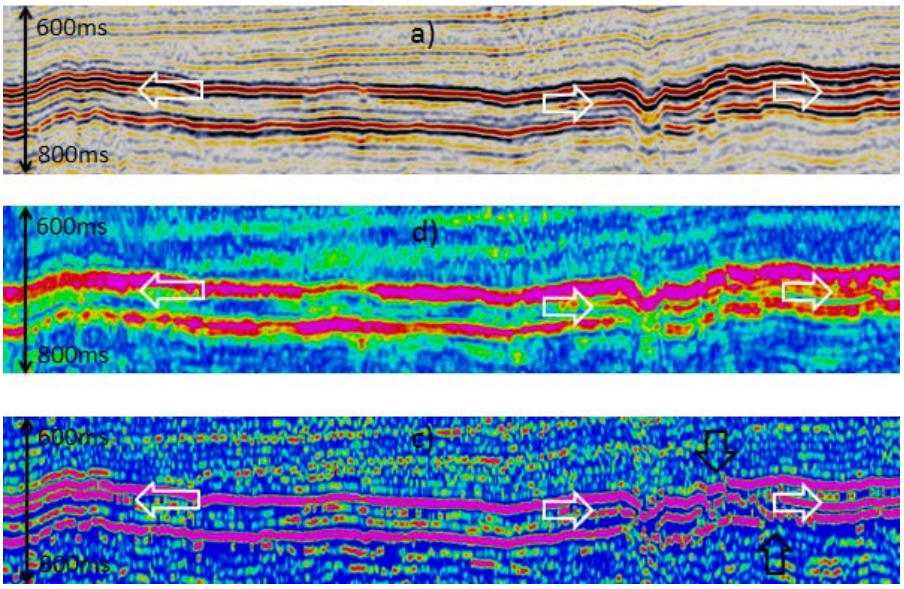

Figure 29. Comparing original data, DFT, and CLSSA results: a) original seismic amplitude data; b) DFT amplitude spectrum using 40ms Hann-window; and, c) CLSSA amplitude spectrum using 40ms Hann-window.

As compared to DFT and CWT techniques, CLSSA shows better resolution of discontinuities in a time slice view (Figure 30). In addition, as compared to other seismic attributes, the isofrequency results of spectral analysis reveal lithology changes, which correspond to the reflection coefficient contrast in the seismic data (Figure 31). As Castagna *et al.* (2003) suggested, spectral decomposition results should follow criteria: distinct seismic events should appear as distinct events under time-frequency analysis. In other words, the vertical resolution of the time frequency analysis should be comparable to a seismogram. The time duration of an event on the time-frequency analysis should not differ from the time duration on the seismogram.

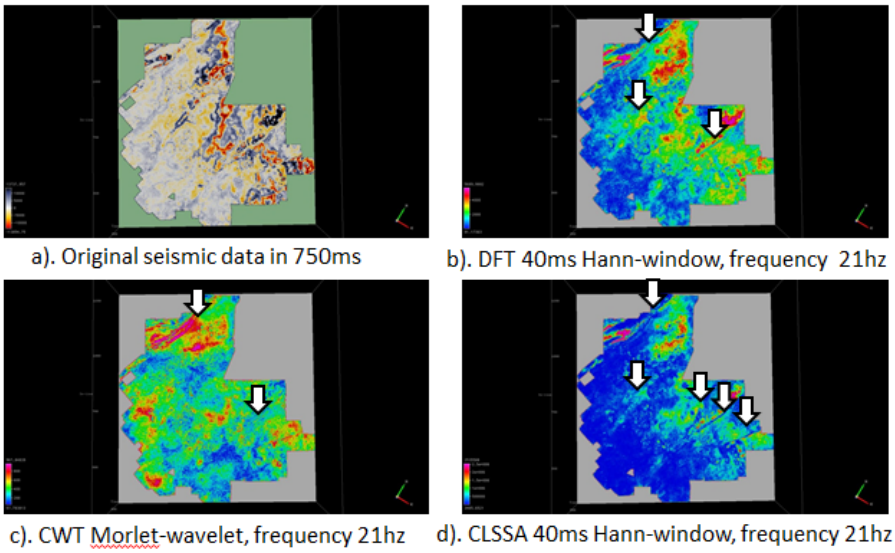

Figure 30. Time slices at 750ms: a) original seismic data; b) DFT result at 21 Hz using 40ms Hann-window; c) CWT at 21 Hz using Morlet-wavelet; and, d) CLSSA at 21 Hz using 40ms Hann-window.

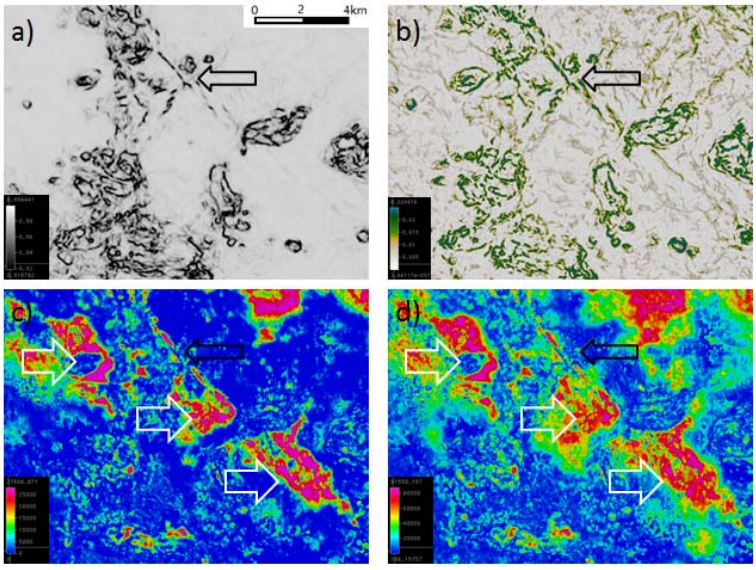

Figure 31. Lithology changes: a) coherency attribute based on cross correlation method; b) fault attribute; c) 20Hz frequency CLSSA result using 20ms Hann-window; and, d) 40Hz frequency CLSSA result using 40ms Hann-window.

4. DISCUSSION

By knowing fault trends and orientation, researchers can find and avoid areas that have high rigidity; they may be more fractured in stress effects. The upper Ellenburger Group is a water-bearing and highly-fractured formation. It is part of a Lower Ordovician carbonate platform sequence that covers a larger area of the United States. Pore networks in the Ellenburger Group are complex because of the amount of brecciation and fracturing associated with karsting. The karsting and fracturing areas greatly affect production from the Barnett Shale because the water could release trapped gas. In Barnett Shale production, it is normally necessary to find a Viola-Simpson limestone layer between Barnett and Ellenburger Formations so that this layer can prevent water from invading from Ellenburger layers into Barnett layers via fractures, faults, and karst. Viola-Simpson limestone does not always provide this buffer because the Barnett Shale extends over an area of 72500 square kilometers in northeast Texas, located within the borders of 17 counties. The CLSSA method is a good spectral analysis technique to detect discontinuities in layers. The fault-detection attribute is calculated using the PCA of different seismic attributes, such as coherency attribute, most positive curvature attribute, variance attribute, smoothed seismic data and isofrequency phase discontinuities volume. Most positive curvature attribute has better resolution compared with other curvature attributes, while coherency attribute is a very good way to map karst-related structures. Phase spectrum is a very good way to detect acoustic impedance changes in lateral way has been used, and some small discontinuities can be detected very well using specific frequency phase maps. The fault-detection attribute can thus reinforce

similar information provided by these attributes and reduce dissimilar information. The use of traditional seismic attributes like coherency attribute and curvature attribute are not good at separating tectonic faults and karsting faults in the low Barnett Shale and top Ellenburger Group. In addition, coherency attribute is not sensitive to faults with a finite offset and curvature attribute is not sensitive to folds and flexures without a discontinuity (Marfurt, 2006). The use of fault attribute as a discontinuity attribute is based on the Barnes (2006) discontinuity-filter method. Its PCA is calculated using different seismic attributes like coherency attribute, positive curvature attribute variance attribute and specific frequency phase map, so that the fault attribute can increase all similar information and reduce dissimilar information. The spectral decomposition method is also effectively applied to geological interpretation and reservoir characterization (Partyka *et al.*, 1999). CLSSA is a better spectral method than the STFT approach because it reduces classical spectral smoothing. Spectral analysis can also highlight stratigraphic characterization.

5. CONCLUSION

In our study, we introduced two unconventional methods for fault detection. Fault attribute used as a dissimilar attribute or discontinuous attribute can easily show small discontinuities or small faults (both karsting-related and tectonic-related) in the Barnett Shale area. Principal Component Analysis (PCA) has been found to be an effective way of combining a variety of fault-detection attributes exhibiting discontinuities that line up along particular 3D orientations. A discontinuity-filter method can be used to further enhance these results. Fault detection is improved using phase discontinuities obtained using a Constrained Least Squares Spectral Analysis (CLSSA) technique, which yields a higher resolution spectral analysis than the short-time Fourier transform (STFT) approach. As CLSSA has reduced spectral smoothing relative to the STFT, it can potentially produce a higher-resolution discontinuity attribute. Based on this feature, CLSSA may be applied in the Barnett Shale to detect faults. Spectral decomposition is a good method for detecting faults that are not evident in seismic amplitude data; this method also shows discontinuities which have a finite offset that are not detected in normal amplitude maps. We compared seismic attributes like coherency attribute, most positive curvature, variance attribute and isofrequency phase maps with the fault-detection attribute. We found that the fault-detection attribute has the best resolution and highest signal to noise ratio. We observe that the fault-detection attribute is a useful attribute in detecting small faults or discontinuities. As compared to coherence and curvature attributes, our PCA fault-attribute also better resolves minor tectonic and karsting-related faults.

6. REFERENCE

Bahorich, M. S., and S. R. Bridges, 1992, The seismic sequence attribute map: 42nd Annual International Meeting, SEG, Expanded Abstracts, p. 227–230.

Bahorich, M. S., and S. L. Farmer, 1995, 3D seismic discontinuity for faults and stratigraphic features: The coherence cube: 65th Annual International Meeting, SEG, Expanded Abstracts, p. 93-96.

Barnes, A. E., 2006, A filter to improve seismic discontinuity data for fault interpretation: Geophysics, 71, p. 1-4.

Bergbauer, S., T. Mukerji, and P. Hennings, 2003, Improving curvature analyses of deformed horizons using scale-dependent filtering techniques: AAPG Bulletin, 87, p. 1255–1272.

Bruner, K. R., and R. Smosna, 2011, A comparative study of the Mississippian Barnett Shale, Fort Worth basin, and Devonian Marcellus Shale, Appalachian basin: Technical Report DOE/NETL/2011/1478, National Energy Technology Laboratory for The United States Department of Energy.

Castagna, J. P., S. Sun, and R. W. Siegfried, 2003, Instantaneous spectral analysis: Detection of low-frequency shadows associated with hydrocarbons: The Leading Edge, 22, p. 102-120.

Chakraborty, A., and D. Okaya, 1995, Frequency-time decomposition of seismic data using wavelet-based methods: Geophysics, 60, p. 1906–1916.

Gersztenkorn, A., and K. J. Marfurt, 1999, Eigenstructure-based coherence computations as an aid to 3-D structural and stratigraphic mapping: Geophysics, 64, p. 1468–1479.

Gulunay, N., and N. Benjamin, 2008, Poststack driven prestack deconvolution for noisy land data and radial trace mixing for signal enhancement: 78th Annual International Meeting, SEG, Expanded Abstracts, p. 2507-2510.

Hart, B. S., R. Pearson, R. Pearson, and G. C. Rawling, 2002, 3D seismic horizon-based approaches to fracture-swarm sweet spot definition in tight-gas reservoirs: The Leading Edge, 21, p. 28–35.

Last, B. J., and K. Kubik, 1983, Compact gravity inversion: Geophysics, 48, p. 713-721.

Lisle, R. J., 1994, Detection of zones of abnormal strains in structures using Gaussian curvature analysis: AAPG Bulletin, 78, p. 1811–1819.

Loucks, R. G., and S. C. Ruppel, 2007, Mississippian Barnett Shale: lithofacies and depositional setting of a deep-water shale-gas succession in the Fort Worth Basin, Texas: AAPG Bulletin, 91, p. 579–601.

Marfurt, K. J., 2006, Seismic Attribute Mapping of Structure and Stratigraphy: Presented at the 2006 EAGE and SEG Meeting, the Distinguished Instructor short Course.

Marfurt, K. J., and R. L. Kirlin, 2000, 3-D broad-band estimates of reflector dip and amplitude: Geophysics, 65, p. 304–320.

Marfurt, K. J., V. Sudhakar, A. Gersztenkorn, K. D. Crawford, and S. E. Nissen, 1999, Coherency calculation in the presence of structural dip: Geophysics, 64, p. 104–111.

Marfurt, K. J., R. L. Kirlin, S. H. Farmer, and M. S. Bahorich, 1998, 3-D seismic attributes using a running window semblance-based algorithm: Geophysics, 63, p. 1150–1165.

Masaferro, J. L., M. Bulnes, J. Poblet, and M. Casson, 2003, Kinematic evolution and fracture prediction of the Valle Morado structure inferred from 3D seismic data, Salta Province, northwest Argentina: AAPG Bulletin, 87, p. 1083–1104.

Montgomery, S. L., D. M. Jarvie, K. A. Bowker, and R. M. Pollastro, 2005, Mississippian Barnett Shale, Fort Worth basin, north-central Texas: Gas-shale play with multi-trillion cubic foot potential: AAPG Bulletin, 89, p. 155–175.

Partyka, G. A., J. A. Gridley, and J. A. Lopez, 1999, Interpretational aspects of spectral decomposition in reservoir characterization: The Leading Edge, 18, p. 353–360.

Portniaguine, O., and M.S. Zhdanov, 1998, Focusing geophysical inversion images: Geophysics, 64, p. 874-887.

Pollastro, R. M., R. J. Hill, T. A. Ahlbrandt, R. R. Charpentier, T. A. Cook, T. R. Klett, M. E. Henry, and C. J. Schenk, 2003, Assessment of undiscovered oil and gas resources of the Bend Arch–Fort Worth Basin province of north-central Texas and southwestern Oklahoma: U.S. Geological Survey National Assessment of Oil and Gas Fact Sheet 2004-3022.

Puryear, C. I., O. N. Portniaguine, C. M. Cobos, and J. P. Castagna, 2012, Constrained least-squares spectral analysis: Application to seismic data: Geophysics, 77, p. 143-167.

Roberts, A., 2001, Curvature attributes and their application to 3-D interpreted horizons: First Break, 19, p. 85–100.

Shlens, J., 2009, A tutorial on principal component analysis: Center for Neural Science, New York University.

Sigismondi, M. E., and J. C. Soldo, 2003, Curvature attributes and seismic interpretation: Case studies from Argentina basins: The Leading Edge, 22, p. 1122-1126.

Tikhonov, A. N., and V.Y. Arsenin, 1977, Solutions of Ill-Posed Problems: V.H. Winston and Sons.

Tingdahl, K., and N. Hemstra, 2003, Estimating fault-attribute orientation with gradient analysis, principal component analysis and the localized Hough-transform: 73rd Annual International Meeting, SEG, Expanded Abstracts, p. 358–361.

Treitel, S., J. L. Shanks, and C. W. Frasier, 1967, Some aspects of fan filter: Geophysics, 32, p. 789-800.